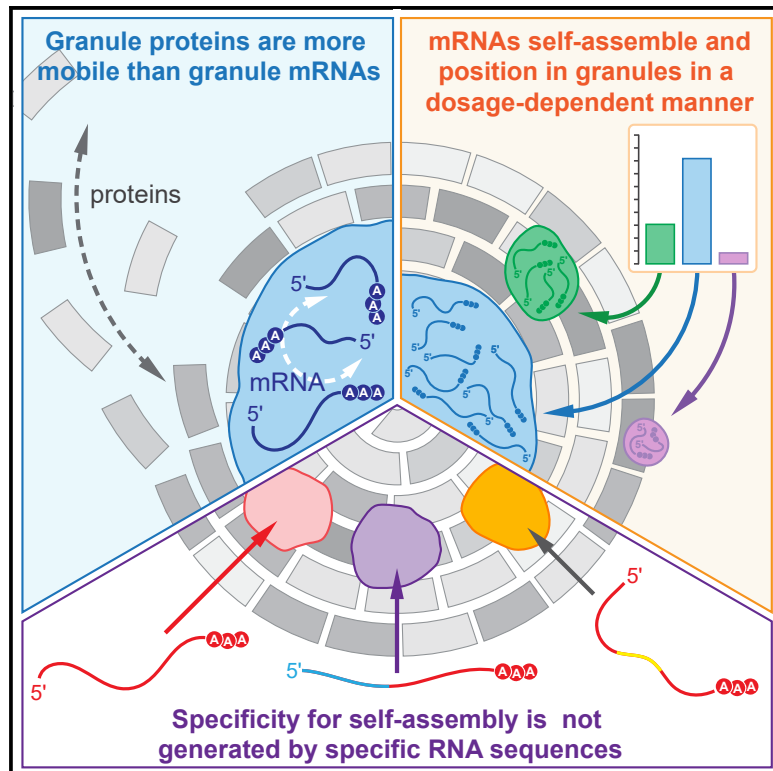


Sequence-Independent Self-Assembly of Germ Granule mRNAs into Homotypic Clusters

Graphical Abstract



Authors

Tatjana Trcek, Tyler E. Douglas, Markus Grosch, ..., Hari Shroff, Eli Rothenberg, Ruth Lehmann

Correspondence

ttrcekp1@jhu.edu (T.T.),
ruth.lehmann@med.nyu.edu (R.L.)

In Brief

mRNAs enriched in *Drosophila* germ granules form homotypic assemblies. *In vivo*, this assembly is not specified by germ granule proteins but instead relies on the mRNA. mRNA self-assembly involves the entire mRNP and is RNA sequence independent and sequence specific. Ordered intermolecular RNA:RNA interactions among clustered transcripts were not observed.

Highlights

- Germ-granule-enriched mRNA organization was probed by super-resolution imaging *in vivo*
- Many mRNAs from the same gene self-assemble into homotypic clusters in germ granules
- Homotypic self-assembly relies on properties of an mRNP, but not specific RNA sequences
- Sequence-specific *trans*-RNA:RNA interactions among clustered mRNAs are not detected



Short Article

Sequence-Independent Self-Assembly of Germ Granule mRNAs into Homotypic Clusters

Tatjana Trcek,^{1,5,*} Tyler E. Douglas,^{1,6} Markus Grosch,^{1,7} Yandong Yin,² Whitby V.I. Eagle,³ Elizabeth R. Gavis,³ Hari Shroff,⁴ Eli Rothenberg,² and Ruth Lehmann^{1,8,*}¹HHMI, Skirball Institute of Biomolecular Medicine, Department of Cell Biology, NYU School of Medicine, New York, NY, USA²Department of Biochemistry and Pharmacology, NYU School of Medicine, New York, NY, USA³Department of Molecular Biology, Princeton University, Princeton, NJ, USA⁴Section on High Resolution Optical Imaging, National Institute of Biomedical Imaging and Bioengineering, NIH, Bethesda, MD, USA⁵Present address: Department of Biology, Johns Hopkins University, Baltimore, MD, USA⁶Present address: Department of Integrative Biology, University of California, Berkeley, Berkeley, CA, USA⁷Present address: Helmholtz Zentrum, München, Germany⁸Lead Contact*Correspondence: trcekp1@jhu.edu (T.T.), ruth.lehmann@med.nyu.edu (R.L.)<https://doi.org/10.1016/j.molcel.2020.05.008>

SUMMARY

mRNAs enriched in membraneless condensates provide functional compartmentalization within cells. The mechanisms that recruit transcripts to condensates are under intense study; however, how mRNAs organize once they reach a granule remains poorly understood. Here, we report on a self-sorting mechanism by which multiple mRNAs derived from the same gene assemble into discrete homotypic clusters. We demonstrate that *in vivo* mRNA localization to granules and self-assembly within granules are governed by different mRNA features: localization is encoded by specific RNA regions, whereas self-assembly involves the entire mRNA, does not involve sequence-specific, ordered intermolecular RNA:RNA interactions, and is thus RNA sequence independent. We propose that the ability of mRNAs to self-sort into homotypic assemblies is an inherent property of a messenger ribonucleoprotein (mRNP) that is augmented under conditions that increase RNA concentration, such as upon enrichment in RNA-protein granules, a process that appears conserved in diverse cellular contexts and organisms.

INTRODUCTION

RNAs, like other biopolymers, tend to assemble both *in vivo* and *in vitro* (Eno et al., 2019; Khong et al., 2017; Little et al., 2015; Pitchiaya et al., 2019; Roovers et al., 2018; Trcek et al., 2015) through the process of phase separation (Eisenberg and Felsenfeld, 1967; Jain and Vale, 2017; Langdon et al., 2018; Van Treeck et al., 2018). In most cases, the molecular principles that allow RNA assembly have not been experimentally determined; however, RNA binding proteins (RBPs), non-Watson-Crick interactions, and promiscuous Watson-Crick and sequence-specific *trans* RNA:RNA interactions have been implicated in driving RNA self-assembly (Eisenberg and Felsenfeld, 1967; Jain and Vale, 2017; Langdon et al., 2018; Van Treeck et al., 2018). Experimentally, three RNAs have been shown to assemble via direct base pairing *in vivo*: the RNA genome of the human immunodeficiency virus (HIV) and the *Drosophila oskar* (*osk*) and *bicoid* (*bcd*) mRNP transport messenger ribonucleoprotein (mRNP) particles. These RNAs use distinct palindromic sequences presented by conserved stem-loop structures to homodimerize (Ferrandon et al., 1997; Jambor et al., 2015; Moore and Hu, 2009; Marquet et al., 1991). Depending on the cellular environ-

ment, RNA structures can hide or expose interacting sequences and thus spatially control RNA assembly in cells (Langdon et al., 2018). Understanding the principles of RNA assembly *in vivo* within the endogenous cellular context is critical in determining how these assemblies shape the biology of a cell.

We have previously shown that upon enrichment into germ granules, the *Drosophila CycB*, *nanos* (*nos*), *polar granule component* (*pgc*), and *germ-cell-less* (*gcl*) mRNAs form homotypic clusters that contain multiple transcripts derived from the same gene (Little et al., 2015; Trcek et al., 2015). These clusters are demixed from one another and located at distinct positions within the homogeneously distributed protein environment of the granule (Trcek et al., 2015). Germ granules, composed of homogeneously mixed core granule proteins Oskar (Osk), Vasa, Aubergine (Aub), and Tudor (Tud), are up to 500 nm in diameter (Arkov et al., 2006) and contain territories occupied by homotypic mRNA clusters (Trcek et al., 2015). The centers harbor core granule proteins and the *CycB* clusters, whereas the *gcl* clusters position at the granule boundary (Trcek et al., 2015). Using *in vivo* quantitative super-resolution microscopy and single-molecule fluorescence *in situ* hybridization (smFISH), combined with genetic manipulations, we show that homotypic



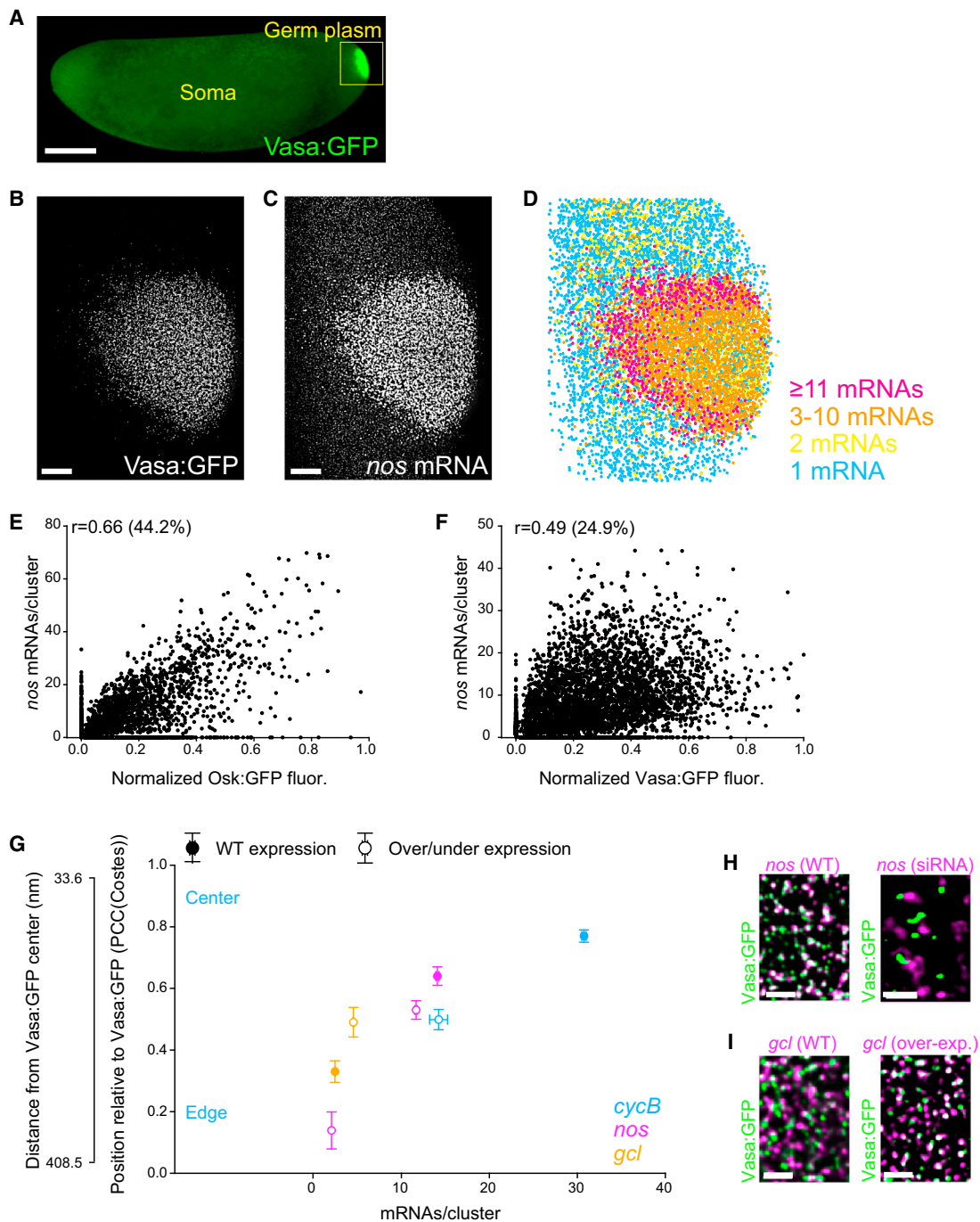


Figure 1. mRNAs Self-Sort into Homotypic Clusters

(A) Embryo with a maternally expressed Vasa:GFP transgene. (B and C) smFISH reveals the spatial distribution of *nos* (C) in germ granules (B). (D) Spatial distribution of *nos* clusters at the posterior pole. (E and F) Correlation of *nos* cluster abundance with the Osk:GFP protein (E) and Vasa:GFP protein (F) abundance quantified by the PCC (r). Each dot represents one granule. %, coefficient of determination. $\geq 3,483$ granules/pair were analyzed. (G) Position and abundance of *CycB* (empty blue circles), *nos* (empty magenta circles), and *gcl* (empty yellow circles) clusters in over- and under-expression experiments and in WT condition (full blue, magenta, and yellow circles, respectively) in Vasa:GFP granules. 33.6 nanometer (nm) on the y axis indicates co-

(legend continued on next page)

assemblies are common among germ-granule-enriched mRNAs and that granule proteins are critically important during this process because clustering does not occur outside of granules. However, once in granules, mRNAs self-assemble into clusters. In contrast to the sequence-driven recruitment of mRNAs by germ granule proteins (Rangan et al., 2009; Gavis et al., 1996; Eagle et al., 2018), the specificity for homotypic mRNA self-assembly is independent of specific RNA sequences, their associated proteins or conserved RNA structures, and core granule proteins. Stochastic optical reconstruction microscopy (STORM) (Rust et al., 2006) measurements support a model in which contacts among clustered mRNAs in granules are independent of any spatially constrained interaction *in trans*. We propose that granule proteins increase mRNA concentration by recruiting them to granules, thereby increasing the probability of mRNAs to self-recognize and self-sort. Thus, the propensity of mRNAs to homotypically assemble is an inherent property of an mRNA, independent of its sequence, and occurs when mRNAs become sufficiently crowded, such as upon their enrichment in RNA condensates. Our *in vivo* work uncovers a transcript-specific yet sequence-independent organizing principle of cellular mRNAs, which could be applicable to diverse RNA condensates across the organismal spectrum.

RESULTS

mRNAs Self-Sort into Homotypic Clusters in Germ Granules

To visualize germ granule mRNAs, we coupled smFISH with structured illumination microscopy (SIM) (York et al., 2013), a super-resolution approach, to quantify mRNA cluster abundance (number of mRNAs/homotypic cluster) both within granules demarcated by the Vasa:GFP signal and outside (Figures 1A–1D and S1A–S1E) (Little et al., 2015; Trcek et al., 2015). We found that clustering was common among granule-enriched mRNAs and that mRNA cluster abundance varied among genes without a defined stoichiometry (Figure S1F; Table S1). Clustering only occurred within granules regardless of the somatic mRNA concentration (Table S1) and thus depended on the ability on an mRNA to enrich in granules (Little et al., 2015; Trcek et al., 2015). Furthermore, cluster abundance only moderately correlated with protein abundance of core granule proteins (Figures 1E, 1F, and S1G), suggesting that mRNA cluster abundance depends on factors other than the core germ granule components (Niepielko et al., 2018).

To determine which mRNA property best predicted the position of clusters within granules, we evaluated parameters that may influence RNA regulation and behavior while using the Pearson correlation coefficient-Costes (PCC[Costes]) approach to determine the position of clusters within Vasa:GFP granules (Figure S2A; STAR Methods) (Trcek et al., 2015). We determined that the strongest positive indicator for the positioning of RNA clusters

within germ granules was mRNA cluster abundance ($r = 0.88$) (Figures S2A and S2B; STAR Methods). For example, *CycB* clusters, with a mean abundance of 30.8 ± 0.2 *CycB* mRNAs, were located in the center of granules (PCC[Costes] of 0.77 ± 0.02) (Figure 1G, full blue circle; Table S1) (Trcek et al., 2015); *nos* clusters with a mean abundance of 14.1 ± 0.2 were located in the middle (PCC[Costes] of 0.64 ± 0.02) (Figure 1G, full magenta circle; Table S1) (Trcek et al., 2015); and *gcl* clusters with a mean abundance of 2.9 ± 0.1 resided at the edge of granules (PCC[Costes] of 0.33 ± 0.04) (Figure 1G, full yellow circle; Table S1) (Trcek et al., 2015). The different cluster positions within granules could not be explained by the differences in their physical size (in square nanometers), because mRNAs that position differently within granules nevertheless form clusters of a similar physical size (Trcek et al., 2015). These results, which extended to all germ-granule-enriched mRNAs tested (Figure S2B), suggested that the abundance of homotypic clusters and hence the concentration of mRNAs within granules could determine the position of mRNA clusters within germ granules.

To test this hypothesis, we manipulated the expression levels of *CycB*, *nos*, and *gcl* to drive the formation of more abundant or less abundant clusters and determined their position within granules. By using RNAi to reduce total embryonic *nos* levels, we decreased the average *nos* cluster abundance from 14.1 ± 0.2 to 2.1 ± 0.2 mRNAs per cluster and recorded that *nos* clusters moved toward the edge of granules in a dosage-dependent manner: from PCC(Costes)_{*nos*-WT} of 0.64 ± 0.03 to PCC(Costes)_{*nos*-RNAi} of 0.14 ± 0.06 (Figures 1G, full and empty magenta circles, and 1H; Figures S2E and S2F). This change was specific for *nos* RNAi-induced under-expression, because RNAi against mCherry transcripts caused no change in the abundance of *nos* mRNA or in the position of *nos* clusters in Vasa:GFP-labeled granules (Figures S2E and S2G). Less drastic under-expression of *nos*, using embryos derived from *nos*^{BN/+} mothers expressing *nos* from only one wild-type (WT) gene copy, decreased the average *nos* cluster abundance to 11.7 ± 0.1 mRNAs and moved *nos* clusters toward the edge of granules (PCC[Costes]_{*nos*^{BN/+}} of 0.53 ± 0.03) (Figure 1G, full and empty magenta circles; Figures S2E and S2F). Similarly, when we decreased the *CycB* cluster abundance from 30.8 ± 0.2 to 14.2 ± 1.0 mRNAs using RNAi, we recorded that *CycB* clusters moved toward the periphery of granules in a dosage-dependent manner: from PCC(Costes)_{*CycB*-WT} of 0.77 ± 0.02 to PCC(Costes)_{*CycB*-RNAi} of 0.49 ± 0.03 (Figure 1G, full and empty blue circles; Figures S2H–S2J). Conversely, when we increased the *gcl* cluster abundance from 2.9 ± 0.1 to 4.5 ± 0.1 by overexpressing *gcl*, *gcl* clusters moved toward the center of the granule: from PCC(Costes)_{*gcl*-WT} of 0.33 ± 0.04 to PCC(Costes)_{*gcl*-over-exp} of 0.49 ± 0.05 (Figures 1G, open and empty yellow circles, and 1I; Figures S2K and S2L). All these changes were statistically significant (Figures S2F, S2J, and S2L). Apart from the changes in the overall concentration and cluster abundance of tested mRNAs, other germ

localization of a doubly labeled *pgc* with itself, and 408.5 nm shows co-localization between Vasa:GFP and non-granule-enriched *ccr4* (Trcek et al., 2015). PCC(Costes) in over- and under-expression assays: mean \pm SEM of 3 embryos/gene. Cluster abundance: 337 to 3,178 clusters/gene/condition.

(H) Co-localization of *nos* (magenta) with Vasa:GFP granules (green) in WT embryos and embryos treated with RNAi against *nos*.

(I) Co-localization of *gcl* (magenta) with Vasa:GFP granules (green) in WT embryos and embryos overexpressing *gcl*.

Scale bar: (C and D) 2 μ m, (B) 10 μ m, and (A) 50 μ m. See also Figures S1 and S2 and Table S1.

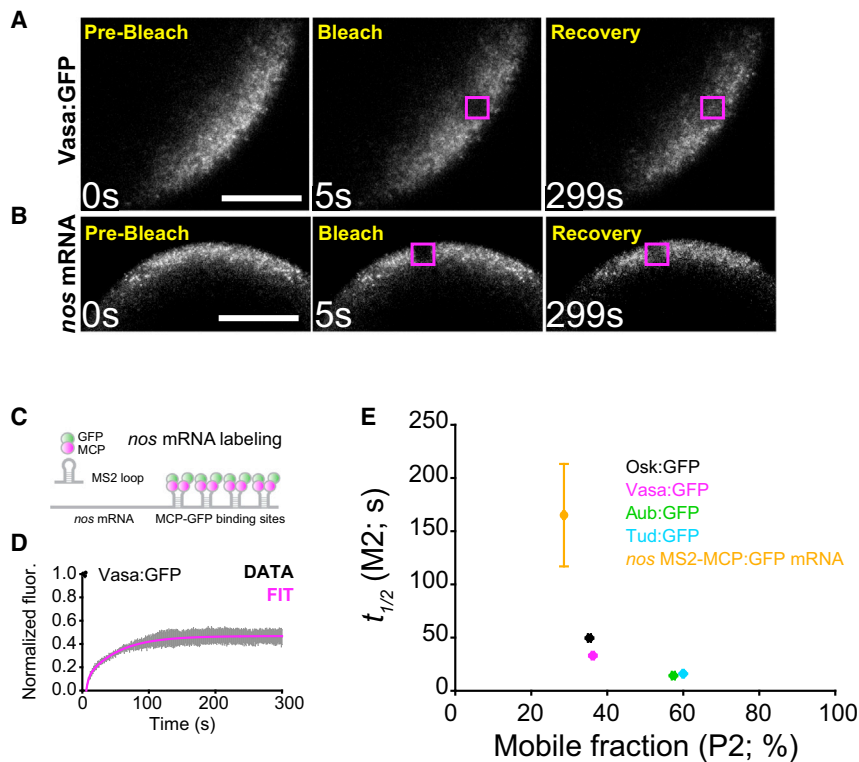


Figure 2. Germ Granule Proteins Are More Mobile Than Germ Granule mRNAs

(A and B) Fluorescence recovery of Vasa:GFP (A) and nos MS2-MCP:GFP (B) after photobleaching a region of interest (ROI) (magenta square) within germ plasm.

(C) Labeling of nos with MS2-MCP:GFP.

(D) Recovery of Vasa:GFP (mean \pm SD, gray bars) of 5 normalized recovery curves. Magenta line, fit to the data.

(E) Kinetics of fluorescence recovery of core granule proteins and nos. The half-time to recovery ($t_{1/2}$, in seconds) and the mobile fraction (percentage of the population that exchanged between granule and intergranular space) is shown.

Mean \pm SD of 5 Osk:GFP, 5 Vasa:GFP, 12 Tud:GFP, 9 Aub:GFP, and 5 nos MS2-MCP:GFP recovery curves. Scale bar represents 10 μ m. See also Figure S3 and Table S2.

granule parameters, such as the average amount of Vasa:GFP in granules, appeared unaffected (Figure S2M).

To probe the effect of mRNA localization on cluster position within granules, we analyzed the spatial distribution of chimeric nos clusters that localize to the posterior less efficiently than endogenous nos clusters (Gavis et al., 1996). In these chimeras, the nos 5' UTR and nos open reading frame (ORF) were fused with the tubulin 3' UTR containing different segments of the nos 3' UTR (here termed nos-tub B, C, or D chimeras) (Figure S2N), which had previously been identified as partially redundant determinants of nos localization to germ granules (Gavis et al., 1996). These chimeras expressed lower overall levels of RNA and enriched less efficiently at the posterior pole than the endogenous nos chimeras (Gavis et al., 1996). Consistently, the three nos-tub chimeras formed less abundant clusters ranging from 2.2 ± 0.3 (nos-tub B) to 3.6 ± 0.6 (nos-tub C) mRNAs (Figure S2O) located at the granule's periphery (Figures S2O and S2P).

Collectively, our analysis revealed that *in vivo*, a given germ-granule-enriched mRNA can occupy any position within the granule and that the position depends on the concentration of the mRNA in germ granules, as well as the effectiveness of its localization to germ granules. Surprisingly, the position is not driven by germ granule proteins but relies directly on the mRNA. We conclude that germ granule mRNAs self-instruct sorting into homotypic clusters.

Germ Granule Proteins Are More Mobile Than Germ Granule mRNAs

The ability of granule mRNAs to self-organize suggests that these mRNAs could display properties distinct from those of

core granule proteins, such as their mobility. To this end, we used fluorescence recovery after photobleaching (FRAP) assays to record how GFP-tagged Osk, Vasa, Aub, and Tud, as well as MS2-MCP:GFP-tagged nos mRNA, exchanged with the granule environment in live embryos (Figures 2A and 2B; STAR Methods).

Our FRAP analysis showed that $35.8\% \pm 0.4\%$, $36.2\% \pm 0.3\%$, $60.0\% \pm 0.2\%$, and $57.4\% \pm 0.6\%$ of Osk, Vasa, Tud, and Aub exchanged with the intergranular space, respectively, with slow kinetic half-lives ($t_{1/2}$) of 49.5 ± 3.7 s (Osk), 33.0 ± 0.9 s (Vasa), 14.2 ± 0.6 s (Tud), and 16.0 ± 0.4 s (Aub) (Figure 2E; Table S2). We found that only between 1.4% (Osk:GFP) and 16.0% (Tud:GFP) of the protein were located in the intergranular space, whereas most were located in granules (Figures 2E and S3C; Table S2) (Kistler et al., 2018). The mobilities recorded for these four proteins in the intergranular space were similar to the mobility of free cytoplasmic GFP protein recorded in follicle cells of stage 11 *Drosophila* oocytes, which do not form germ plasm (Figure S3D; Table S2). Therefore, in the intergranular space, the mobility of Osk, Vasa, Tud, and Aub seemed unrestricted. Vasa displayed a similar mobility to Osk, whereas Aub was similar to Tud (Figure 3E; Table S2), an anticipated result given that Osk recruits and physically interacts with Vasa in granules (Breitwieser et al., 1996), whereas Tud recruits and physically interacts with Aub (Liu et al., 2010; Kirino et al., 2010).

Strikingly, nos-MS2-MCP:GFP mRNA was less mobile than any assayed proteins (mobile fraction of $28.6\% \pm 0.2\%$ and $t_{1/2}$ of 165.0 ± 48.1 s) (Figure 3E; Table S2). This slower mobility is not caused by the propensity of MCP:GFP to retain in granules, because in the absence of nos-MS2 mRNA, this protein does not accumulate in granules (Figure S3E). In addition, this kinetic of exchange may be over-estimated given that we were detecting the exchange of MCP:GFP protein bound to the nos-MS2 mRNA rather than the mobility of nos mRNA. We conclude that *in vivo*, granule-enriched nos mRNA is stably associated within granules and far less mobile than any of the four core

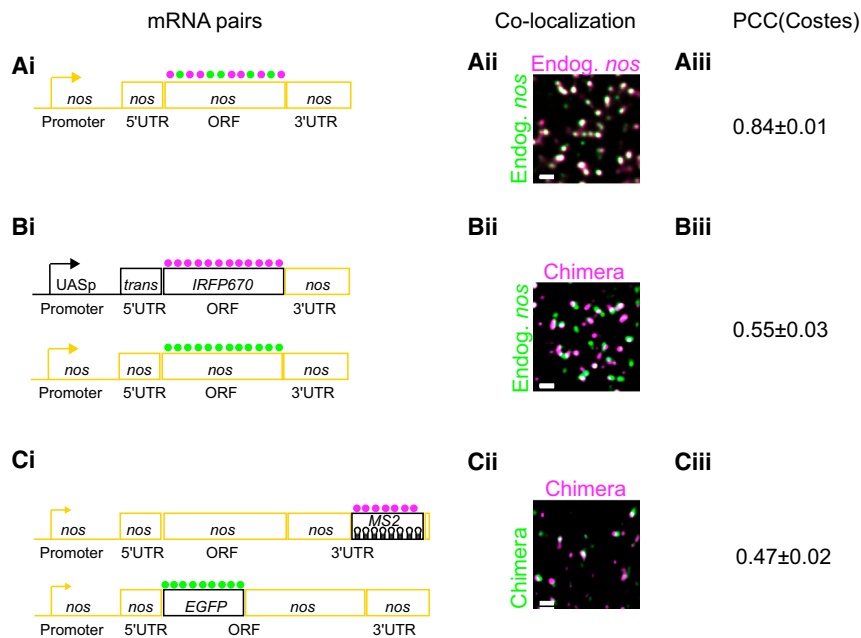


Figure 3. Self-Assembly into Homotypic Clusters Is RNA Sequence Independent

(A) Endogenous *nos* hybridized with spectrally distinct smFISH probes (i), displaying high co-localization (ii), with a PCC(Costes) of 0.84 ± 0.01 (mean \pm SEM of 5 embryos) (iii). (B) Endogenous *nos* and the *nos* 3' UTR chimera hybridized with distinct probes (i), poorly co-localized (ii), with a PCC(Costes) of 0.55 ± 0.03 (mean \pm SEM of 6 embryos) (iii). (C) Two full-length *nos* chimeras hybridized with distinct probes (i), poorly co-localized (ii), with a PCC(Costes) of 0.47 ± 0.02 (mean \pm SEM of 6 embryos) (iii). Scale bar represents 1 μ m. See also Tables S3 and S4.

granule proteins. Thus, mRNAs such as *nos* display slower mobilities from those of core granule proteins and constitute the stable component of germ granules.

Self-Assembly into Homotypic Clusters Is RNA Sequence Independent

To understand how mRNAs self-assemble, we sought to identify the part of the RNA that generates specificity for homotypic clustering. We speculated that if embryos expressed two mRNAs that shared features needed to co-assemble but were otherwise distinct, the two transcripts would highly co-localize with each other within the same cluster. Alternatively, if the two mRNAs did not share such features, they may localize to the same granule but organize two distinct homotypic clusters that would poorly co-localize with each other.

To test this hypothesis, we focused on *nos* mRNA whose localization signals, like those of several other germ granule mRNAs, reside in its 3' UTRs (Rangan et al., 2009; Gavis et al., 1996; Eagle et al., 2018). We reasoned that the determinants required for homotypic *nos* assembly could also reside in its 3' UTR. To this end, we constructed chimeras that only shared the *nos* 3' UTR with the endogenous gene and fused it to an ORF of a far-red fluorescent protein (IRFP670), which allowed the simultaneous detection of the chimeric mRNA and the endogenous *nos* within the same granule using distinct smFISH probes (Figure 3B, i). To define co-localization of multiple *nos* molecules within the same cluster, we stained the endogenous *nos* with two sets of spectrally distinct smFISH probes (Figure 3A, i) and detected high co-localization (Figure 3A, ii) with a PCC(Costes) of 0.84 ± 0.01 (Figure 3A, iii). This value establishes the expected co-localization coefficient should two distinct *nos* transcripts sort into the same cluster.

Our measurements revealed that although the chimeric *nos* formed abundant clusters (Table S3), it displayed a low co-localization coefficient with endogenous *nos* (PCC(Costes) of $0.55 \pm$

0.03) and thus organized into distinct clusters within the same granule (Figure 3B, ii and iii). We measured a similar low PCC(Costes) between chimeras fused with the *gcl* or *pgc* 3' UTRs and their respective endogenous counterparts (Tables S3 and S4). The low co-localization coefficient of the *nos* 3' UTR reporter with the endogenous *nos* could not be attributed to the IRFP670 ORF, because clusters of the *nos* chimera, in which the *nos* 3' UTR was fused with the ORF of EGFP and the actin-interacting domain of the moesin protein (Moe:EGFP) (Edwards et al., 1997) also co-localized with endogenous *nos* with a low PCC(Costes) (Tables S3 and S4). Therefore, the 3' UTRs of germ granule mRNAs, although required for their recruitment to granules, were insufficient to generate the specificity for mRNA sorting into homotypic clusters within granules.

To determine whether other mRNA features regulate self-assembly, we tested chimeras fused with the 5' UTR of *nos*, *pgc*, and *gcl*, as well as the promoter of *nos*, and found that these too sorted independently from their respective endogenous counterparts (Tables S3 and S4). Finally, we analyzed two chimeras that had all the features of the endogenous *nos* (5' and 3' UTRs, ORF, and introns and whose expression was driven by the *nos* promoter) but differed in heterologous sequences inserted into these complete transcripts, which allowed binding of spectrally distinct smFISH probes and differentiation of the two chimeras within the same granule. The first chimera carried 18 MS2 RNA loops inserted at the end of *nos* 3' UTR (Brechtel and Gavis, 2008), whereas the ORF of the second was fused with EGFP (Figure 3C, i) (Forrest et al., 2004). The fluorescence originating from the EGFP reporter was minimal and did not interfere with the fluorescence originating from Alexa 488 smFISH probes (Figures S3F and S3G). Importantly, these MS2 and EGFP chimeras fully rescue the *nos* null phenotype (Sinsimer et al., 2013; Forrest et al., 2004) indicating that the relevant regulatory elements of endogenous *nos*, including its structured translational control element, were preserved in both chimeras. Our experiments revealed that although the two chimeras formed abundant mRNA clusters within the same granules (Table S3), they sorted into distinct clusters with a low PCC(Costes) of 0.47 ± 0.02 (Figure 3C, ii and iii; Table S4).

Lastly, we speculated that the length of a transcript could generate the specificity for self-sorting. Nevertheless, *CycB*, *nos*, and *gcl* mRNAs, which have similar lengths (2,556, 2,349, and 2,464 nucleotides [nt], respectively) (Table S3), organized into distinct clusters (Figures 1G and S2A) (Trcek et al., 2015), whereas *nos* chimeras fused with Moe:EGFP or with IRFP670, which also had a length similar to that of endogenous *nos* similarly organized into distinct clusters (Tables S3 and S4).

In the context of a full-length *nos* sequence, the insertion of heterologous sequences is sufficient to cause demixing. This strongly suggests that *nos* lacks essential and mappable regions required to generate specificity for homotypic assembly. This finding is therefore inconsistent with a model in which the homotypic mRNA assembly would be driven by direct, sequence-specific *trans* mRNA-mRNA base pairing or recognition via proteins deposited on specific *nos* mRNA features. Instead, our data argue that the features of the entire mRNA, including unrelated, heterologous sequences, contribute to the specificity of sorting.

mRNA Organization within Homotypic Clusters Is Disordered

Our genetic data demonstrate that the specificity for mRNA self-assembly does not require distinct RNA sequences. Therefore, mRNAs in clusters are likely unrestricted by any sequence-encoded, *trans* RNA:RNA interaction, and contacts between clustered transcripts may be less stereotypical than those between mRNAs bound by specific sequence complementarity. To address this possibility *in vivo*, we characterized the spatial organization of mRNAs within homotypic clusters and transport mRNPs using STORM (Figures S4A–S4E). We reasoned that if we hybridized a single probe conjugated to a photoswitchable dye within the region of the mRNA that engages in sequence-specific *trans* RNA:RNA interaction, for instance, with sequences located within its 3' UTR, then this intermolecular interaction will spatially constrain that region to a small cluster radius (Figure 4A). Conversely, if a probe is hybridized to the region of the mRNA that does not engage in sequence-specific *trans* RNA:RNA interactions, then that region would be expected to be less spatially constrained and would create areas with a larger cluster radius (Figure 4A). However, for mRNAs within homotypic assemblies that do not rely on specific sequences for their association, we would expect that no specific mRNA region would be spatially constrained and that all probes would report cluster radii of similar sizes, regardless of their position on the mRNA (Figure 4B).

To determine whether we could detect sequence-specific *trans* RNA:RNA interactions, we examined *osk* mRNA. *osk* localizes to the posterior pole via kinesin motors but does not enrich in germ granules (Trcek et al., 2015; Little et al., 2015; Lehmann, 2016). Its 3' UTR harbors a stem-loop structure, which contains a palindrome that promotes *osk* dimerization (Figure 4E, i and ii) (Jambor et al., 2011). As a result, localized *osk* forms clusters at the posterior pole that in the early embryo on average contained 21.8 ± 0.5 mRNAs (Figure S4G).

When single smFISH probes hybridized to the *osk* 5' UTR, ORF, or the beginning of its 3' UTR, we detected cluster radii ranging from 50.1 ± 5.4 to 55.9 ± 12.4 nm (Figure 4C). The measurement of the clusters' physical size was invariant of the type of the pho-

toswitchable dye, because probes coupled to Alexa 647 or Alexa 568 produced cluster radii of similar sizes (Figure 4C, radii marked with green and magenta circles). However, when probes hybridized directly adjacent to *osk*'s palindrome, we recorded a smaller cluster radius of 31.4 ± 11.1 nm, a statistically significant 40% decrease (Figure 4C). Using the mean cluster radius determined by STORM and cluster abundance measured by smFISH and SIM, we calculated the mean compactness of *osk* clusters (mean volume derived from the radius of a cluster occupied by one *osk* mRNA) at various positions. We found that outside of the palindrome, *osk* transcripts within the cluster were far less compact than within the palindromic region (mean compactness of 2.8 ± 0.4 and 0.6 ± 0.1 , respectively) (Figure S4H). These data also imply that potential non-specific RNA:RNA interactions among *osk* molecules outside of the palindrome cannot spatially constrict *osk* mRNPs as effectively as a single RNA region engaged in direct sequence-specific base pairing. Notably, we were able to record this constriction *in situ*, although *osk* is translated at the posterior pole (Kim-Ha et al., 1995; Gunkel et al., 1998). Thus, the ribosome-crowded environment of *osk* clusters did not preclude smFISH probes from hybridizing to *osk* or prevent photoswitching of fluorescent dyes, firmly validating STORM as a tool to characterize *trans* RNA:RNA interactions *in vivo*. Our direct observation at the posterior pole of the embryo revealed that *osk* mRNPs are spatially constrained within their 3' UTR, where *osk* engages in sequence-specific and ordered *trans* RNA:RNA interactions, and showed a more relaxed configuration along regions of the RNA not engaged in sequence-specific *trans* RNA:RNA interactions.

We next employed the same strategy to the analysis of *nos* clusters. In contrast to *osk*, we did not observe specific constriction of the cluster radius, regardless of where on the *nos* mRNA we hybridized smFISH probes and despite an average concentration of *nos* within clusters that was 4,761 times higher than outside of granules (Table S5). Instead, we recorded an average cluster radius of 42.9 ± 7.4 nm (Figure 4D) with an average compactness of 2.4 ± 1.2 (Figure S4H). This compactness was similar to that recorded for *osk* mRNA outside of its palindromic region (Figure S4H). In addition, we analyzed *gcl* mRNA and recorded a mean cluster radius of 35.4 ± 2.3 nm and a mean compactness of 6.5 ± 1.2 across the length of the *gcl* transcript (Figures 4H and 4I). As with *osk*, these measurements were not influenced by the choice of the photoswitchable dye that was conjugated to the probes (Figures 4D and S4I, radii marked with green and magenta circles). We conclude that unlike *osk*, *in vivo* clustered *nos* and *gcl* are not engaged in sequence-specific base pairing and that contacts between these mRNAs are not stereotypical, consistent with our genetic data (Figure 3). We conclude that spatial organization among clustered transcripts in *Drosophila* germ granules is disordered.

DISCUSSION

In this study, we addressed the molecular parameters of homotypic mRNA assembly within RNA granules *in vivo*. Our data suggest that models relying on specific *trans* RNA:RNA interactions generated by RBPs or by base-paired RNA sequences observed for *osk* and *bcd* mRNPs and the HIV genome cannot explain the

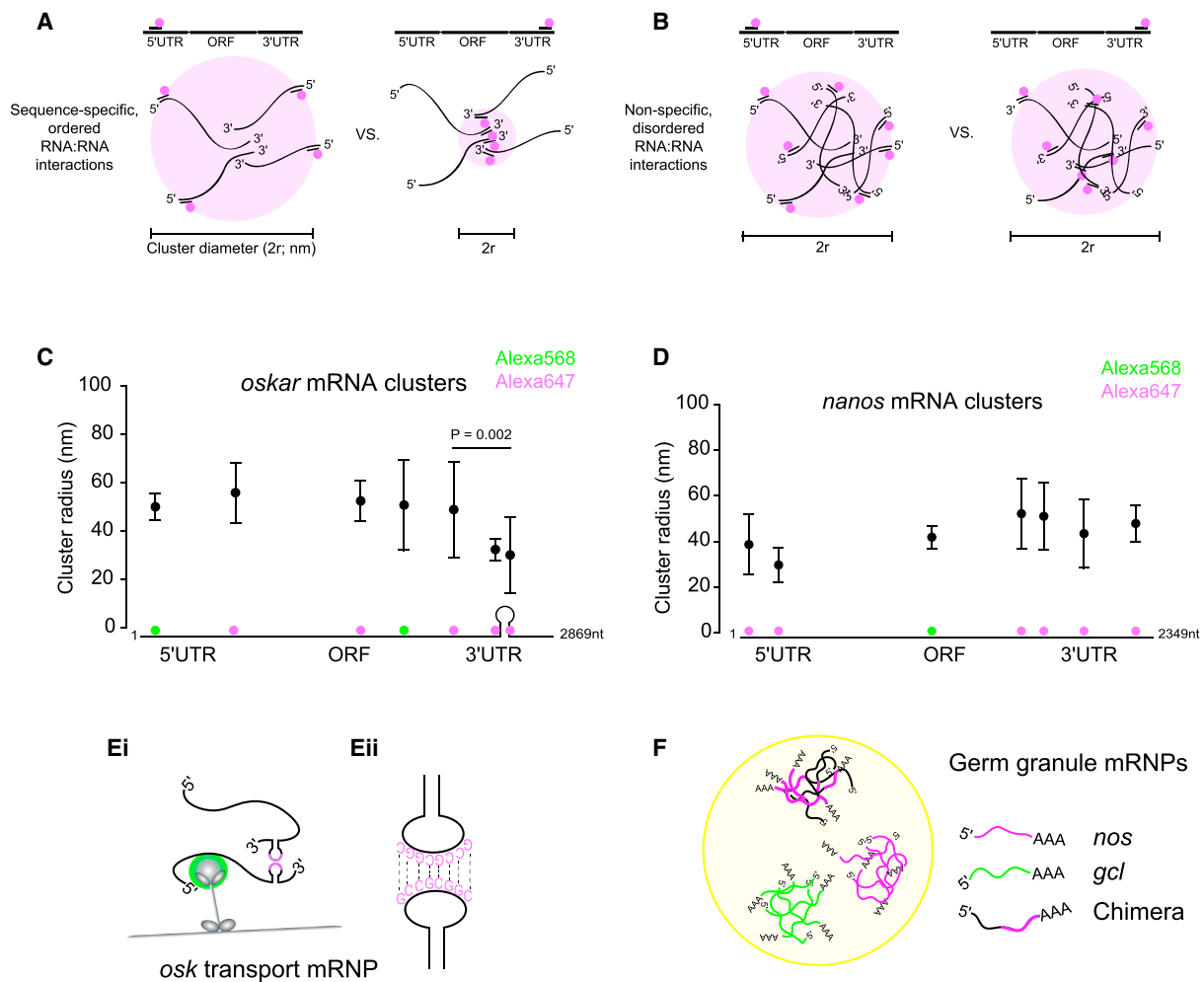


Figure 4. mRNA Organization within Homotypic Clusters Is Disordered

(A and B) Detection scheme of sequence-specific, ordered (A) and non-specific, disordered (B) *trans* RNA:RNA interactions using smFISH (magenta circle) and STORM. In (A), mRNAs base pair in a sequence-dependent manner with their 3' UTRs and become spatially constrained (right panel) compared with the 5' UTR that do not base pair (left panel). Magenta dot, smFISH probes; magenta circles, cluster radius recorded by STORM. (B) In the absence of sequence-specific, ordered *trans* RNA:RNA interactions, the same radius of mRNA clusters is recorded regardless of the position of the smFISH probe hybridization. For simplicity, mRNAs are drawn as linear polymers in (A) and (B).

(C) Radii of *osk* clusters. Statistical significance p, two-tailed t test. Magenta and green circles are Alexa 647 and Alexa 568 probes, respectively. Per probe, mean \pm SD of 11 to 30 ROIs is plotted, with localization uncertainty of 15.5 ± 6.2 to 26.6 ± 2.6 nm.

(D) Radii of *nos* clusters. Magenta and green circles are Alexa 647 or Alexa 568 probes, respectively. Per probe, mean \pm SD of 17 to 40 ROIs is plotted with localization uncertainty of 12.4 ± 4.3 to 20.7 ± 2.2 nm.

(E) *osk* mRNA transport particle coupled to a dynein motor (i) (Sanghavi et al., 2013) and homodimerized via a palindromic sequence (ii) (Jambor et al., 2011).

(F) Germ granule mRNAs distinguish among distinct mRNAs as well as near-cognate mRNAs.

See also Figure S4 and Tables S5 and S6.

specificity for homotypic mRNA assembly in *Drosophila* germ granules. Instead, we show that RNA:RNA interactions among clustered *nos* and *gcl* are sequence independent and disordered.

The exact molecular mechanism of homotypic mRNA self-assembly is not clear; however, it is distinct from the localization principles that generally rely on the 3' UTR-encoded features for enrichment of mRNAs in germ granules (Figure 3). Because RNA modifications are typically sequence encoded (Roundtree et al., 2017), these similarly are likely not providing the specificity

for homotypic assembly. Furthermore, accumulation of *nos*, *CycB*, *pgc*, and *gcl* occurs concurrently (Little et al., 2015), indicating that *nos* chimeras expressed from the same promoter arrive at granules simultaneously; therefore, different time of arrival of transcripts cannot give rise to demixed clusters within granules. Similarly, full-length *nos* transgenes tagged with EGFP or MS2 loops were inserted at multiple genomic loci, and their mRNAs each demixed into a single distinct cluster, excluding the possibility that epigenetic mRNA imprinting could drive homotypic assembly. In addition, given that the position of

clusters changes simply when cluster mRNA abundance is altered independently of granule protein composition (Figure 1G), it is unlikely that granule proteins other than core proteins could drive homotypic assembly. Most compelling, a protein-driven model would have predicted that full-length *nos* chimeras, which only differed in their EGFP or MS2 tag, would be recognized by the same *trans* factors and thus organize into the same cluster, a model not supported by our *in vivo* measurements (Figure 3C). Lastly, the specificity for self-assembly could be generated by distinct RNA structures that could control self-assembly (Langdon et al., 2018). Such RNA structures are expected to be encoded by conserved RNA sequences (Clever et al., 1996; Ferrandon et al., 1997; Jambor et al., 2011). However, *nos* chimeras that included all *nos* sequences but differed in their tags demixed from one another (Figure 3C, i). This suggests that neither sequence-specific RNA:RNA interactions nor specific structural RNA elements are generating the specificity for homotypic clustering. A recent study suggested that RNAs could self-recruit to stress granules and revealed that *in vitro* transcribed *nos*, *pgc*, and *gcl* RNAs interact with one another, suggesting that sequence-specific base pairing could give rise to homotypic mRNA assembly (Tauber et al., 2020). Although this *in vitro* study cannot account for the sequence-independent mRNA sorting into homotypic assemblies we observed *in vivo*, it might explain how RNA:RNA interactions initially recruit these transcripts to germ granules. Indeed, *nos*, *pgc*, and *gcl* have been proposed to self-recruit to granules (Niepielko et al., 2018), possibly via specific *trans* RNA:RNA interactions.

Given that RNAs phase separate *in vitro* (Eisenberg and Felsenfeld, 1967; Van Treeck et al., 2018; Jain and Vale, 2017; Langdon et al., 2018) and *in vivo* (Jain and Vale, 2017), it is possible that homotypic RNA assemblies could form by phase separation according to their miscible properties. Instead of a single determinant such as an RNA sequence or fold, the miscibility of an mRNA could be specified by its many features, including bound proteins, modifications, structures, and length. Thus, granule mRNAs could read the sum of all of characteristics to discriminate between transcripts rather than rely on one single determinant. In this global approach, if an mRNA becomes altered, so would the sum of its features, causing even near-cognate transcripts to sort into distinct clusters. mRNPs that share their primary sequences but are distinctly modified, structured, or protein bound could also sort into distinct clusters. Thus, chimeras that contained all *nos* sequences but were modified by EGFP or MS2 repeats have a different sum of their features, becoming differently miscible and sorting distinctly.

Finally, rather than sorting toward one another, mRNAs could simply sort away from transcripts that are different. Future experiments are required to decipher the mechanistic principles that govern the specificity of this mRNA sorting *in vivo*.

STAR★METHODS

Detailed methods are provided in the online version of this paper and include the following:

- KEY RESOURCES TABLE
- RESOURCE AVAILABILITY

- Lead Contact
- Materials Availability
- Data and Code Availability
- EXPERIMENTAL MODEL AND SUBJECT DETAILS
 - Fly lines
- METHOD DETAILS
 - Microscopes
 - Embryo collection
 - Single-molecule fluorescent *in situ* hybridization (smFISH)
 - mRNA concentration and cluster abundance measurements using smFISH
 - Correlating mRNA properties with the position of mRNA clusters in germ granules
 - Correlating mRNA cluster abundance with the abundance of granule proteins
 - Quantifying co-localization using PCC(Costes)
 - Quantifying total embryonic mRNA levels using qRT-PCR
 - Fluorescence recovery after photobleaching (FRAP)
 - Hybridizing cut embryos with smFISH probes for imaging with STORM
 - Imaging of smFISH-labeled samples using STORM
 - Single-Molecule Localization
 - Pair-Correlation Analysis
- QUANTIFICATION AND STATISTICAL ANALYSIS

SUPPLEMENTAL INFORMATION

Supplemental Information can be found online at <https://doi.org/10.1016/j.molcel.2020.05.008>.

ACKNOWLEDGMENTS

We thank Alexey Soshnev for preparation of the graphical abstract, Harshad Vishwasrao and Jiji Chen of the trans-NIH advanced imaging and microscopy facility for their assistance with the instant structural illumination microscope (iSIM), and Benjamin Lin for help with cloning. This work was supported by the Howard Hughes Medical Institute, where R.L. is an investigator, through K99HD088675 (to T.T.); the Intramural Research Programs of the US NIBIB (H.S.), through R01 GM067758 (to E.R.G.); and NIH training grant T32 GM007388 (to W.V.I.E.).

AUTHOR CONTRIBUTIONS

Conceptualization, T.T. and R.L.; Methodology, T.T., E.R., and R.L.; Investigation, T.T., T.E.D., M.G., E.R.G., and W.V.I.E.; Formal Analysis, T.T., T.E.D., and M.G.; Validation, T.T., T.E.D., and Y.Y.; Software, T.T., T.E.D., Y.Y., E.R., and H.S.; Writing – Original Draft, T.T.; Writing – Review & Editing, T.T., R.L., T.E.D., M.G., Y.Y., H.S., and E.R.G.; Funding Acquisition, T.T. and R.L.; Resources, T.T., E.R., H.S., E.R.G., and R.L.; Supervision, T.T., E.R., and R.L.

DECLARATION OF INTERESTS

H.S. receives royalties, as co-inventor, from sales of iSIM by Visitech. The NIH, its officers, and staff do not recommend or endorse any company, product, or service.

Received: November 14, 2019

Revised: February 29, 2020

Accepted: May 5, 2020

Published: May 27, 2020

REFERENCES

- Arkov, A.L., Wang, J.Y., Ramos, A., and Lehmann, R. (2006). The role of Tudor domains in germline development and polar granule architecture. *Development* **133**, 4053–4062.
- Bergsten, S.E., and Gavis, E.R. (1999). Role for mRNA localization in translational activation but not spatial restriction of nanos RNA. *Development* **126**, 659–669.
- Bertrand, E., Chartrand, P., Schaefer, M., Shenoy, S.M., Singer, R.H., and Long, R.M. (1998). Localization of ASH1 mRNA particles in living yeast. *Mol. Cell* **2**, 437–445.
- Bolte, S., and Cordelières, F.P. (2006). A guided tour into subcellular colocalization analysis in light microscopy. *J. Microsc.* **224**, 213–232.
- Brangwynne, C.P., Eckmann, C.R., Courson, D.S., Rybarska, A., Hoegge, C., Gharakhani, J., Jülicher, F., and Hyman, A.A. (2009). Germline P granules are liquid droplets that localize by controlled dissolution/condensation. *Science* **324**, 1729–1732.
- Brechbiel, J.L., and Gavis, E.R. (2008). Spatial regulation of nanos is required for its function in dendrite morphogenesis. *Curr. Biol.* **18**, 745–750.
- Breitwieser, W., Markussen, F.H., Horstmann, H., and Ephrussi, A. (1996). Oskar protein interaction with Vasa represents an essential step in polar granule assembly. *Genes Dev.* **10**, 2179–2188.
- Cinalli, R.M., and Lehmann, R. (2013). A spindle-independent cleavage pathway controls germ cell formation in *Drosophila*. *Nat. Cell Biol.* **15**, 839–845.
- Clever, J.L., Wong, M.L., and Parslow, T.G. (1996). Requirements for kissing-loop-mediated dimerization of human immunodeficiency virus RNA. *J. Virol.* **70**, 5902–5908.
- Costes, S.V., Daelemans, D., Cho, E.H., Dobbin, Z., Pavlakis, G., and Lockett, S. (2004). Automatic and quantitative measurement of protein-protein colocalization in live cells. *Biophys. J.* **86**, 3993–4003.
- Curd, A., Cleasby, A., Makowska, K., York, A., Shroff, H., and Peckham, M. (2015). Construction of an instant structured illumination microscope. *Methods* **88**, 37–47.
- Eagle, W.V.I., Yeboah-Kordieh, D.K., Niepielko, M.G., and Gavis, E.R. (2018). Distinct *cis*-acting elements mediate targeting and clustering of *Drosophila* polar granule mRNAs. *Development* **145**, dev164657.
- Edwards, K.A., Demsky, M., Montague, R.A., Weymouth, N., and Kiehart, D.P. (1997). GFP-moesin illuminates actin cytoskeleton dynamics in living tissue and demonstrates cell shape changes during morphogenesis in *Drosophila*. *Dev. Biol.* **191**, 103–117.
- Eisenberg, H., and Felsenfeld, G. (1967). Studies of the temperature-dependent conformation and phase separation of polyriboadenylic acid solutions at neutral pH. *J. Mol. Biol.* **30**, 17–37.
- Eno, C., Hansen, C.L., and Pelegri, F. (2019). Aggregation, segregation, and dispersal of homotypic germ plasm RNPs in the early zebrafish embryo. *Dev. Dyn.* **248**, 306–318.
- Ferrandon, D., Koch, I., Westhof, E., and Nüsslein-Volhard, C. (1997). RNA-RNA interaction is required for the formation of specific bicoid mRNA 3' UTR-STAU-FEN ribonucleoprotein particles. *EMBO J.* **16**, 1751–1758.
- Forbes, A., and Lehmann, R. (1998). Nanos and Pumilio have critical roles in the development and function of *Drosophila* germline stem cells. *Development* **125**, 679–690.
- Forrest, K.M., and Gavis, E.R. (2003). Live imaging of endogenous RNA reveals a diffusion and entrapment mechanism for nanos mRNA localization in *Drosophila*. *Curr. Biol.* **13**, 1159–1168.
- Forrest, K.M., Clark, I.E., Jain, R.A., and Gavis, E.R. (2004). Temporal complexity within a translational control element in the nanos mRNA. *Development* **131**, 5849–5857.
- Gavis, E.R., Curtis, D., and Lehmann, R. (1996). Identification of *cis*-acting sequences that control nanos RNA localization. *Dev. Biol.* **176**, 36–50.
- Gunkel, N., Yano, T., Markussen, F.H., Olsen, L.C., and Ephrussi, A. (1998). Localization-dependent translation requires a functional interaction between the 5' and 3' ends of oskar mRNA. *Genes Dev.* **12**, 1652–1664.
- Huang, F., Hartwich, T.M., Rivera-Molina, F.E., Lin, Y., Duim, W.C., Long, J.J., Uchil, P.D., Myers, J.R., Baird, M.A., Mothes, W., et al. (2013). Video-rate nanoscopy using sCMOS camera-specific single-molecule localization algorithms. *Nat. Methods* **10**, 653–658.
- Jain, A., and Vale, R.D. (2017). RNA phase transitions in repeat expansion disorders. *Nature* **546**, 243–247.
- Jambor, H., Brunel, C., and Ephrussi, A. (2011). Dimerization of oskar 3' UTRs promotes hitchhiking for RNA localization in the *Drosophila* oocyte. *RNA* **17**, 2049–2057.
- Jambor, H., Surendranath, V., Kalinka, A.T., Mejschik, P., Saalfeld, S., and Tomancak, P. (2015). Systematic imaging reveals features and changing localization of mRNAs in *Drosophila* development. *eLife* **4**, e05003.
- Jeske, M., Bordi, M., Glatt, S., Müller, S., Rybin, V., Müller, C.W., and Ephrussi, A. (2015). The Crystal Structure of the *Drosophila* Germline Inducer Oskar Identifies Two Domains with Distinct Vasa Helicase- and RNA-Binding Activities. *Cell Rep.* **12**, 587–598.
- Kadyrova, L.Y., Habara, Y., Lee, T.H., and Wharton, R.P. (2007). Translational control of maternal Cyclin B mRNA by Nanos in the *Drosophila* germline. *Development* **134**, 1519–1527.
- Khong, A., Matheny, T., Jain, S., Mitchell, S.F., Wheeler, J.R., and Parker, R. (2017). The Stress Granule Transcriptome Reveals Principles of mRNA Accumulation in Stress Granules. *Mol. Cell* **68**, 808–820.
- Kim-Ha, J., Kerr, K., and Macdonald, P.M. (1995). Translational regulation of oskar mRNA by bruno, an ovarian RNA-binding protein, is essential. *Cell* **81**, 403–412.
- Kirino, Y., Vourekas, A., Sayed, N., de Lima Alves, F., Thomson, T., Lasko, P., Rappalber, J., Jongens, T.A., and Mourelatos, Z. (2010). Arginine methylation of Aubergine mediates Tudor binding and germ plasm localization. *RNA* **16**, 70–78.
- Kistler, K.E., Trcek, T., Hurd, T.R., Chen, R., Liang, F.X., Sall, J., Kato, M., and Lehmann, R. (2018). Phase transitioned nuclear Oskar promotes cell division of *Drosophila* primordial germ cells. *eLife* **7**, e37949.
- Köhler, K., and Domdey, H. (1991). Preparation of high molecular weight RNA. *Methods Enzymol.* **194**, 398–405.
- Kronja, I., Yuan, B., Eichhorn, S.W., Dzeyk, K., Krijgsveld, J., Bartel, D.P., and Orr-Weaver, T.L. (2014). Widespread changes in the posttranscriptional landscape at the *Drosophila* oocyte-to-embryo transition. *Cell Rep.* **7**, 1495–1508.
- Langdon, E.M., Qiu, Y., Ghanbari Niaki, A., McLaughlin, G.A., Weidmann, C.A., Gerbich, T.M., Smith, J.A., Crutchley, J.M., Termini, C.M., Weeks, K.M., et al. (2018). mRNA structure determines specificity of a polyQ-driven phase separation. *Science* **360**, 922–927.
- Lehmann, R. (2016). Germ Plasm Biogenesis—An Oskar-Centric Perspective. *Curr. Top. Dev. Biol.* **116**, 679–707.
- Lionnet, T., Czaplinski, K., Darzacq, X., Shav-Tal, Y., Wells, A.L., Chao, J.A., Park, H.Y., de Turris, V., Lopez-Jones, M., and Singer, R.H. (2011). A transgenic mouse for *in vivo* detection of endogenous labeled mRNA. *Nat. Methods* **8**, 165–170.
- Little, S.C., Sinsimer, K.S., Lee, J.J., Wieschaus, E.F., and Gavis, E.R. (2015). Independent and coordinate trafficking of single *Drosophila* germ plasm mRNAs. *Nat. Cell Biol.* **17**, 558–568.
- Liu, H., Wang, J.Y., Huang, Y., Li, Z., Gong, W., Lehmann, R., and Xu, R.M. (2010). Structural basis for methylarginine-dependent recognition of Aubergine by Tudor. *Genes Dev.* **24**, 1876–1881.
- Livak, K.J., and Schmittgen, T.D. (2001). Analysis of relative gene expression data using real-time quantitative PCR and the 2^{-ΔΔC_T} Method. *Methods* **25**, 402–408.
- Mahowald, A.P. (2001). Assembly of the *Drosophila* germ plasm. *Int. Rev. Cytol.* **203**, 187–213.

- Marquet, R., Baudin, F., Gabus, C., Darlix, J.L., Mougel, M., Ehresmann, C., and Ehresmann, B. (1991). Dimerization of human immunodeficiency virus (type 1) RNA: stimulation by cations and possible mechanism. *Nucleic Acids Res.* **19**, 2349–2357.
- Moore, M.D., and Hu, W.S. (2009). HIV-1 RNA dimerization: It takes two to tango. *AIDS Rev.* **11**, 91–102.
- Nemoz, C., Ropars, V., Frit, P., Gontier, A., Drevet, P., Yu, J., Guerois, R., Pitois, A., Comte, A., Deltell, C., et al. (2018). XLF and APLF bind Ku80 at two remote sites to ensure DNA repair by non-homologous end joining. *Nat. Struct. Mol. Biol.* **25**, 971–980.
- Niepielko, M.G., Eagle, W.V.I., and Gavis, E.R. (2018). Stochastic Seeding Coupled with mRNA Self-Recruitment Generates Heterogeneous *Drosophila* Germ Granules. *Curr. Biol.* **28**, 1872–1881.
- Pae, J., Cinalli, R.M., Marzio, A., Pagano, M., and Lehmann, R. (2017). GCL and CUL3 Control the Switch between Cell Lineages by Mediating Localized Degradation of an RTK. *Dev. Cell.* **42**, 130–142.
- Pitchiaya, S., Mourao, M.D.A., Jaliha, A.P., Xiao, L., Jiang, X., Chinnaiyan, A.M., Schnell, S., and Walter, N.G. (2019). Dynamic Recruitment of Single RNAs to Processing Bodies Depends on RNA Functionality. *Mol. Cell.* **74**, 521–533.
- Rangan, P., DeGennaro, M., Jaime-Bustamante, K., Coux, R.X., Martinho, R.G., and Lehmann, R. (2009). Temporal and spatial control of germ-plasm RNAs. *Curr. Biol.* **19**, 72–77.
- Rapsomaniki, M.A., Kotsantis, P., Symeonidou, I.E., Giakoumakis, N.N., Taraviras, S., and Lygerou, Z. (2012). easyFRAP: an interactive, easy-to-use tool for qualitative and quantitative analysis of FRAP data. *Bioinformatics* **28**, 1800–1801.
- Roovers, E.F., Kaaij, L.J.T., Redl, S., Bronkhorst, A.W., Wiebrands, K., de Jesus Domingues, A.M., Huang, H.Y., Han, C.T., Riemer, S., Dosch, R., et al. (2018). Tdrd6a Regulates the Aggregation of Buc into Functional Subcellular Compartments that Drive Germ Cell Specification. *Dev. Cell.* **46**, 285–301.
- Rørth, P. (1998). Gal4 in the *Drosophila* female germline. *Mech. Dev.* **78**, 113–118.
- Roundtree, I.A., Evans, M.E., Pan, T., and He, C. (2017). Dynamic RNA Modifications in Gene Expression Regulation. *Cell* **169**, 1187–1200.
- Roy, S., Ernst, J., Kharchenko, P.V., Kheradpour, P., Negre, N., Eaton, M.L., Landolin, J.M., Bristow, C.A., Ma, L., Lin, M.F., et al.; modENCODE Consortium (2010). Identification of functional elements and regulatory circuits by *Drosophila* modENCODE. *Science* **330**, 1787–1797.
- Rust, M.J., Bates, M., and Zhuang, X. (2006). Sub-diffraction-limit imaging by stochastic optical reconstruction microscopy (STORM). *Nat. Methods* **3**, 793–795.
- Sanghavi, P., Laxani, S., Li, X., Bullock, S.L., and Gonsalvez, G.B. (2013). Dynein associates with oskar mRNPs and is required for their efficient net plus-end localization in *Drosophila* oocytes. *PLoS ONE* **8**, e80605.
- Sengupta, P., Jovanovic-Taliman, T., Skoko, D., Renz, M., Veatch, S.L., and Lippincott-Schwartz, J. (2011). Probing protein heterogeneity in the plasma membrane using PALM and pair correlation analysis. *Nat. Methods* **8**, 969–975.
- Sinsimer, K.S., Lee, J.J., Thiberge, S.Y., and Gavis, E.R. (2013). Germ plasm anchoring is a dynamic state that requires persistent trafficking. *Cell Rep.* **5**, 1169–1177.
- Sonoda, J., and Wharton, R.P. (2001). *Drosophila* Brain Tumor is a translational repressor. *Genes Dev.* **15**, 762–773.
- Staller, M.V., Yan, D., Randklev, S., Bragdon, M.D., Wunderlich, Z.B., Tao, R., Perkins, L.A., Depace, A.H., and Perrimon, N. (2013). Depleting gene activities in early *Drosophila* embryos with the “maternal-Gal4-shRNA” system. *Genetics* **193**, 51–61.
- Tauber, D., Tauber, G., Khong, A., Van Treeck, B., Pelletier, J., and Parker, R. (2020). Modulation of RNA Condensation by the DEAD-Box Protein eIF4A. *Cell* **180**, 411–426.
- Thomsen, S., Anders, S., Janga, S.C., Huber, W., and Alonso, C.R. (2010). Genome-wide analysis of mRNA decay patterns during early *Drosophila* development. *Genome Biol.* **11**, R93.
- Trcek, T., Chao, J.A., Larson, D.R., Park, H.Y., Zenklusen, D., Shenoy, S.M., and Singer, R.H. (2012). Single-mRNA counting using fluorescent *in situ* hybridization in budding yeast. *Nat. Protoc.* **7**, 408–419.
- Trcek, T., Grosch, M., York, A., Shroff, H., Lionnet, T., and Lehmann, R. (2015). *Drosophila* germ granules are structured and contain homotypic mRNA clusters. *Nat. Commun.* **6**, 7962.
- Trcek, T., Lionnet, T., Shroff, H., and Lehmann, R. (2017). mRNA quantification using single-molecule FISH in *Drosophila* embryos. *Nat. Protoc.* **12**, 1326–1348.
- Tutucci, E., Vera, M., Biswas, J., Garcia, J., Parker, R., and Singer, R.H. (2018). An improved MS2 system for accurate reporting of the mRNA life cycle. *Nat. Methods* **15**, 81–89.
- Van Treeck, B., Protter, D.S.W., Matheny, T., Khong, A., Link, C.D., and Parker, R. (2018). RNA self-assembly contributes to stress granule formation and defining the stress granule transcriptome. *Proc. Natl. Acad. Sci. USA* **115**, 2734–2739.
- Veatch, S.L., Machta, B.B., Shelby, S.A., Chiang, E.N., Holowka, D.A., and Baird, B.A. (2012). Correlation functions quantify super-resolution images and estimate apparent clustering due to over-counting. *PLoS ONE* **7**, e31457.
- Wang, C., Dickinson, L.K., and Lehmann, R. (1994). Genetics of nanos localization in *Drosophila*. *Dev. Dyn.* **199**, 103–115.
- Webster, A., Li, S., Hur, J.K., Wachsmuth, M., Bois, J.S., Perkins, E.M., Patel, D.J., and Aravin, A.A. (2015). Aub and Ago3 Are Recruited to Nuage through Two Mechanisms to Form a Ping-Pong Complex Assembled by Krimper. *Mol. Cell* **59**, 564–575.
- Whelan, D.R., Lee, W.T.C., Yin, Y., Ofri, D.M., Bermudez-Hernandez, K., Keegan, S., Fenyo, D., and Rothenberg, E. (2018). Spatiotemporal dynamics of homologous recombination repair at single collapsed replication forks. *Nat. Commun.* **9**, 3882.
- Yang, N., Yu, Z., Hu, M., Wang, M., Lehmann, R., and Xu, R.M. (2015). Structure of *Drosophila* Oskar reveals a novel RNA binding protein. *Proc. Natl. Acad. Sci. USA* **112**, 11541–11546.
- Yin, Y., Lee, W.T.C., and Rothenberg, E. (2019). Ultrafast data mining of molecular assemblies in multiplexed high-density super-resolution images. *Nat. Commun.* **10**, 1119.
- York, A.G., Chandris, P., Nogare, D.D., Head, J., Wawrzusins, P., Fischer, R.S., Chitnis, A., and Shroff, H. (2013). Instant super-resolution imaging in live cells and embryos via analog image processing. *Nat. Methods* **10**, 1122–1126.
- Zheng, J., Gao, M., Huynh, N., Tindell, S.J., Vo, H.D., McDonald, W.H., and Arkov, A.L. (2016). *In vivo* mapping of a dynamic ribonucleoprotein granule interactome in early *Drosophila* embryos. *FEBS Open Bio* **6**, 1248–1256.

STAR★METHODS

KEY RESOURCES TABLE

REAGENT or RESOURCE	SOURCE	IDENTIFIER
Chemicals, Peptides, and Recombinant Proteins		
TRIzol reagent	Invitrogen	15596018
Acid-phenol:chloroform	Invitrogen	AM9720
Chloroform	Fisher	AC40463-5000
Isopropanol	Fisher Scientific	A416-500
RQ1 RNase-Free DNase	Promega	M6101
Oligo dT(20) primer	Thermo Fisher Scientific	18418020
SuperScript® III Reverse Transcriptase	Life Technologies	18080-044
YBR Green reporter dye	Roche	04707516001
Tissue freezing medium	General Data	TFM-C
Poly-L-lysine solution	Sigma	P4707-50ml
Epoxy	Devcon	00470740
Catalase	Sigma-Aldrich	C3115-50MG
Glucose Oxidase	Sigma-Aldrich	G2133-10KU
IRF670 plasmid	Addgene	45457
Critical Commercial Assays		
AlexaFluor 488 oligonucleotide Amine labeling kit	Life Technologies	A-20191
MicroSpin G-25 Columns	GE Healthcare	27-5325-01
384-well qRT-PCR plates	Roche	04729749001
Plastic disposable molds	Fisherbrand	22-363-552
Cryostat	Leica	CM 3050 S
Low profile blades	Accu-Edge	4689
Experimental Models: Organisms/Strains		
<i>w</i> ¹¹¹⁸ ("wild type")	Bloomington Drosophila Stock Center	5905
pFlyFos-Osk:sfGFP	(Jambor et al., 2015; Trcek et al., 2015)	N/A
<i>y,w</i> ; P[E GFP- <i>vas w</i> ^{+cyIII}]	(Trcek et al., 2015)	N/A
UASp-GFP-Aub	(Webster et al., 2015)	N/A
GFP-Tud	(Zheng et al., 2016)	N/A
::P{GAL4::VP16- <i>nos.UTR</i> }/ <i>TM3Ser</i>	(Pae et al., 2017)	N/A
<i>w</i> ; <i>matα-gal4</i> ; <i>PrDr</i> / <i>TM3</i>	(Pae et al., 2017)	N/A
<i>w</i> ; P(<i>EPgy2</i>) <i>gcl</i> ^{EY09611} / <i>CyO</i> ; <i>nosGal4VP16 (w+)</i> / <i>TM3</i>	(Cinalli and Lehmann, 2013)	N/A
<i>w</i> ; P(<i>EPgy2</i>) <i>gcl</i> ^{EY09611} / <i>CyO</i> ; <i>nosGal4VP16 (w+)</i> / <i>TM3</i>	(Cinalli and Lehmann, 2013)	N/A
<i>nos</i> -(<i>MS2</i>) ₁₈	(Sinsimer et al., 2013)	N/A
<i>hsp83</i> -MCP-GFP	(Forrest and Gavis, 2003)	N/A
<i>nos-tub</i> B,C, D chimeras	(Gavis et al., 1996)	N/A
<i>nos</i> RNAi <i>y</i> ¹ <i>sc</i> [*] <i>v</i> ¹ ; P{ <i>TRiP.HMS00930</i> } <i>attP2</i>	Bloomington Drosophila Stock Center	33973
<i>CycB</i> RNAi <i>y</i> ¹ <i>sc</i> [*] <i>v</i> ¹ ; P{ <i>TRiP.HMS02163</i> } <i>attP2</i> / <i>TM3</i> , <i>Sb</i> ¹	Bloomington Drosophila Stock Center	40915
mCherry RNAi <i>y</i> ¹ <i>sc</i> [*] <i>v</i> ¹ <i>sev</i> ²¹ ; P{ <i>y</i> [+ <i>t</i> 7.7] <i>v</i> [+ <i>t</i> 1.8] = UAS-mCherry.VALIUM10} <i>attP2</i>	Bloomington Drosophila Stock Center	35787
<i>w</i> [*]; P{ <i>w</i> [+ <i>mC</i>] = <i>GAL4-slbo.2.6</i> }1206 P{ <i>w</i> [+ <i>mC</i>] = UAS-GFP.S65T} <i>T2</i> / <i>CyO</i>	Kyoto Stock Center	108-787
<i>ry nos</i> ^{BN} <i>e</i> / <i>TM3 Sb e</i>	(Wang et al., 1994)	N/A
<i>sp</i> / <i>CyO</i> ; <i>nos</i> ^{BN} , <i>Vasa</i> :GFP/ <i>TM3 Ser</i>	This study	N/A
<i>nos</i> ^{Def} (<i>Df</i> (3R) <i>DIFx3</i> / <i>TM3 Sb, Ser</i>)	(Forbes and Lehmann, 1998)	N/A

(Continued on next page)

Continued

REAGENT or RESOURCE	SOURCE	IDENTIFIER
<i>moesin</i> -GFP ORF tagged with <i>nos</i> 3'UTR	(Rangan et al., 2009)	N/A
EGFP ORF-tagged with <i>gcl</i> 3'UTR	(Rangan et al., 2009)	N/A
<i>yw</i> ; P(w ⁺ EGFP- <i>nos</i>) ¹¹ ; P(w ⁺ EGFP- <i>nos</i>) ⁵	(Forrest et al., 2004)	N/A
<i>nosp-5'gcl-EGFP-3'gcl</i> and <i>nosp-5'pgc-EGFP-3'pgc</i>	(Eagle et al., 2018)	N/A
smFISH Probes (5' to 3')		
aret cgtatccagacggaagcagg, aacatctgatgtgtccgg, cgtactcctcgaacatctcg, cgcagaacgttgatcgagtg, aaagcagcaacccttgctaa, gcggcgtgtctcgtataaaa, attatgcaaagcatcctggg, acatcccatttagcgtctta, gggctcatttgaatgggat, cattgcgattctcgctatcg, ataccacaaagagttgctg, ctggtcagcttctgttta, ccgtggacttcaaatagctt, ttggtggcaatgtagcga, ctttaatggccgaaatggca, atgatctgttctggctcag, gtagcggcgaactgacgac, ttccagagattggcctgaat, aggtatgtgatgtgtctgg, aatggcatctcgccgagaa, ctgcagcagttgaatggagg, gtgagggttgcaacaactg, catcggggtcaaaagtctcg, aatggccgtagattctgga, cattcgagagactcggctgc, gatgccattggattcggatc, ggccgctgtgacatatatg, gcgaagtggaactgactg, gcggcagatggtgatgaaa, agatccgatcgggtgaactc, cgagatcacattgcccgaagg, ctgctctgtttgctgatgaa, aaaccggaagcacttcgaca, agtccggattgtcgaaggag, ttctcagctgcacttgag	Stellaris smFISH probes	N/A
tao1 ttgtagccggacatctgttc, taaagttgtggagcagcgtg, tgctgatcctctgctcaag, ttgtgtagtttctctcgg, ttctcctgtttagcgtaat, gtcgactcatcctggagag, tgcgattgcagggtaagatc, agctcgatgtactgctctg, atcatccgtttgctgtgaa, gtggtgcttaagaagcatgg, tgttctgtttatctgctc, tttgattatgcaactcgg, tcttgatgcggtccatgtag, cttttgctcaagctctc, aactgcttgcgtatcggag, ttagcgtttgtattgctc, ttggtgtcgtctgcagtac, ttaatgacctcctctgtt, cgatgctctctcctcag, atgctttgctcgtactgttc, ctgactttggaacatgctcg, ggctttcgtctagttgtag, gtacgttggcactcaatcac, ttctgttctgttctggta, cgattctcgagctcacgacg, tccatcttattctcgagcag, ctggttgaattgctgcaact, tagtagcttctcgtgtttc, ttcgttatcaaatgcttcca, tgctgaaacctagggcaatt, tcgggatacctcaatcagag, attgaaccagacagacttcc, gttgaactattgctatggg, atagcgaaccagccggaaaa, tggcattgtttgtctatg, actaaactgttggggg, tcgcaactgttgctttataa, gatttctgtgctgtgctg, gctctattgatgcttagcg, tgtttctgctgctattgttt, aaacattgctagctagccat, gttgtctcttcttagttc, catgtgtgtttgggtgtg, ccaatccgataattgatcgc, ggttctcatgtttcctaag, tattgcagcttagctgtt, ccgatcgagtttcccttaat, atgttagtatctgttgcca	Stellaris smFISH probes	N/A
pum ctgcgagtagagattctgtt, tcaacgagctcgtgttcaag, tccgaacatattgtggcag, gggattcgagaagatcgagc, cttcgagaaggcgagatctt, gagatcgcgtagctgaagat, cctgtgagaactccacaatg, ttctgttgataaaccgca, atctcgtgaacaccatttg, ctgtagacatagttgcca, ttgacgcatttcagcacatg, cacatgattgccattctgat, acgcactcaatgcacttttg, ttgatgatgaactgcagcgc, tgggtgcttagcagtaaac, ctcaaggattctctggatca, ctcatgcagttcgtccaaaa, acatagttgccatattggtc, gtgttcaagcacatgctgaa, agaatcgacttacctctg, tgatagcaccagaactttg, acgttgagcgaactgtg, catgggtaacacatttctcc, cttcatcatcacgtgcaacg, accacatagttggcactg, aactggcattgatgtgctt, gggattggttattctcatg, accgaacaaatgggtgggta, gcctggctaaattgttatt, tgttaagctctacagcttct, ttatcgctgctttccaata, caaatctcagtgacgctc, tgtgtgtttactatcctc, aagctctttgctttttg, ttatgcgagcgcattttaca, ttcatctttgctgtcatg, gatcgcgatttactacgcat, ttcttttttctcagctcgc, tcgtaggtaattcatgacg, aatggtcctctgctgaac, gttatccctgatatatgt, ctgctggctccaaaaacatt, tctctgtttcattgtgtct, attgtgtgggtgatgcaac, tgaatggcctgaagagctgt, gttgtgtttggggtttt, gaccaaatatcatgcagatc, ttggctacttggtcaaca	Stellaris smFISH probes	N/A

(Continued on next page)

Continued

REAGENT or RESOURCE	SOURCE	IDENTIFIER
<p>elF4G2 attgttgaagtgggggtgt, cgtagtgggaaaggtcaca, aagctgtttctgtgtggag, actgggaatgccaaagtgt, ccaaaataggggtcgatc, caagtgcggagcaaatgtgt, ctgtgttactgacggagtt, ggtactattgtatccagag, acaataacgatgacccccgag, ctgatctgatcittatccgt, cttgtttgtggccaattt, agctgggtaactatcgact, aatactcgacttctgtgtg, gtggaatgctggagttgat, ttctgttttcttccag, gcattgtgctatttgtgt, gaattgaagctgtgctct, gagctcatatgaaacctgt, agcगतatgttttggaacc, ggcacatagtccaatgattc, cttagcagcacctcaagt, cattgtcattttagcctca, ctgaatgcgggtgatcaacg, ttgctgtggcatattac, cgactgcagctgaaaagct, acaaatgacccactgtgtt, tctgcatcataaaccgcac, ttggcatcttctgcatgaa, atctatgcttaggtctgat, agcaattgaatcgctgggtg, aacaaggatgtagggcggagg, gaatgctcatttacttcca, gtgcaaatagctccgtgagta, ccaaacatcttttaggtcca, ctgtacaaactcccgatact, gagtgcaacagctacgggaag, tcgatacacagctgcagtag, tctatgaagcaatcctccag, tacagaacgctgaacgtgtg, tagctataccactgtcga, tcaatgaatggcgacggta, agttgtgtgtgtgtgtg, tggttcaaacgatgtgcc, ctgatctagctatcgtgcaa, tctataccagttcacattg, ttgattgttttgagcca, gctctttgtttgtctttt, ttgattgggttttcattg</p>	Stellaris smFISH probes	N/A
<p>orb tgcaaatctcgactttggc, aggagctttagcgtgtgat, ttgatcagcggcattgttg, cgctcatcaagttaccaaga, ccatttctgcatcagttgat, ccatcgttgggtgtataat, gcagccgaactcttatagaa, ttgagcatacggtgcgaacg, cgaggaagaccttgggagaa, ctactaatatcccaggaa, gctgaagatctggatgagc, gccactccatttaatatag, taacataacccttgggctg, gcttgcgattcaagatt, gccgaaagtaatgccttgac, agaatcatccactgaagca, agaagtgtctaccacag, atacgccgcgaagagatttt, tgactcaacatccttgagc, gagtacgcgataatccaagg, ggagctggatgcacaaaat, caaacacggtttcgttggg, atccattatattccaagc, atctataccagcatacagca, cgatcgggtactgtacttg, ttgctaaatgacacagctcc, cagcttcatataggagcga, taatctgataaaagcgcc, ctcttggtgaactctgtgg, caccgcatatggaacatag, attccctacaatagtaggga, gcagaagatcggagcagc, ttgacgatgtcacagctgtg, acttgagttgcgagtcaag, tcgacgaagatggtccgatg, ggccagagaagggtaacgaa, cattctgttcccgtgata, catcacgttgagactgtggg, ttaccattgatgtagcagc, tgaattgccgctgctgaag, atgctgtgacgctgtatc, agccgtaacagcttagatcg, catccgttaaaccggtgtgg, gtccaagtctcacacatta, catatttctacgtgcctac, ccacggctgcaagaaaact, taatgacgatgatgagcccg, agcttcatattgtaccgata</p>	Stellaris smFISH probes	N/A
<p>CG18446 acgtttctctcgggactaaa, ttaaattcactaggggtgcc, caactgttctgtaggatcgc, ctcttcggttgggtgaatta, tatgatctccacatcgctat, gtggtgatgatggttcatga, ggtatggcggatggaatttg, cagtgggtgaaaatggtggg, gttccttcgggaacatttat, aggtagcacggaacacagag, atcattgaagggctgtttgc, gtgtattccaggcgttaat, acaaaggggttatcgtcgg, ataagtctgatctgtggga, atgtgatggtgatccatgt, cgagcggcgggtgagtaaaaa, atgaaccgcaggcattttaa, ggtggtatctgaatcggatg, tatgctgagcggctatatac, gccgatgacctaaaaactgc, aggagattgcgggtgacattg, atggatgaccagaaggctc, tgtgttacttggatcgc, aggtttgcatttcaagcga, atcctgaatcggatctgtg, aagccaaggatttgcattt, aattgcactcgaactgacct, gctgtgcaaatctctct, ttgatgtgagcacttatg, tcatgtgcatcaggaggaaag, aaagcaatcccgtgtttgac, ttggatattcgggacgagc, cggatcacaggcgaatctaca, cgacattggggagacaggaa, agcgttgaatattcgtgtgc, cgtaaaacccgattccaact, aagtggatagtccgtttgg, agatccggattgaagtaggg, gccaaagtcaacctataagt, gatacccaagcttcttaaa, tggctatcttattagctcga, catagtcagaagctccatga, cttgcgagtcgatgtat, tcgagatccagatccaaagt, caagaagttggggcttttg, atgctcagcgttttagttt, agcgtccgagtgcttaaaat, gcgttcttatttccattt</p>	Stellaris smFISH probes	N/A

(Continued on next page)

Continued

REAGENT or RESOURCE	SOURCE	IDENTIFIER
Shu gcgtttgagaaaaagacttt, agttggcgtattctttgg, aaacgaattccggaatgcgc, gttttctcattatcgcaa, ttgagcaactgtgggtgta, gatccgaataggacaagggga, aactcaacgccccttttcac, catggttctgctgcaattg, tatgtccacggtgacgtag, cgcacgcagttcgtcgaatg, tttcgtgatctcgctcatc, cgagtgatccgcttgaat, cagtagccactgtaccgaac, cagggaggagtgaagggag, tggccagtccaacacgaa, taaggacgatctgctggac, ggagattataaactggcct, aaccgagttctccgaaaagc, cactttaagagcgcatccg, cctatgagcgagtagtcaat, ctgggggatagcatcgatg, cacacaaaactgtcgcggt, atgtaggtgcaagtcgacag, cagttgctgactctgatag, cagtagtctagtagctcac, agtaagcagttcagtttct, gatcatcaggttttggttca, cctgttcatctgtttaa, gtaaggcctcatcatgatg, gaagagcgcctgcaagacg, caagtgtactcgcccagag, ataactcgtcgtgatctc, ctacactgtgattctct, ttaacgagaagcagctgc, tttgcccagctgactttg, ttgaaactctgttctttg, gttctaaaccgctaata, aagctcactgttgatctga, gtcgaactgagcgttcaat, ttcttgccaatttgcaag, gggagacaaagttagctca, atgtcagaacatcctctgg, aagcgaactaaatccggc, tactgggctcttagtaag, ctgctcttagaacttgg, taacattcgtcgggcttac, actaaaggtctacgttgc, gccgtgactattttattg	Stellaris smFISH probes	N/A
sra acgcattgtttggacttg, gtcaggagtggctggatcag, ttgctggagtggctgactg, cagttgttctgtctctgc, cactgctgtctgtctgcac, cgacagctgtctatgctgc, ggccggtgatgaaaatgt, ggagcgacggatgctgattg, tcgtcgaacgagctgcatc, cagcatgattgaggtgggta, aaacacctcggagtggatg, cgtgctcagctctggattg, gaattgcccgaataactcct, cactggaacgtagccgattc, aacacgcaggcgacggaagc, ccgcaatggcattgcatag, cagcttgatcgcgactttg, ccgtctctgttaaaactcg, tgggcaaatgtagcaggtgat, tgcaggtctgttctgac, ggggagatgaggaactgtt, caacggcccaaaaagatcat, atggccgtgtgcacaataat, cactggctggacaattgg, tcaccacctatgattatgc, caggtttcagctttattg, ccgatcgtttgttttaca, aaatactcaatcgaagcccc, gttcagtgcttataatac, ggaagatgctgggtatgg, atgctacgctgaaggaag, tgtatcagaagcactggg, tgcggtgttagccaatgaa, atcgcgagataaacacatct, tctacacatagacacactc, ttgcgatggcttaacatcaa, ttagatattgttagcaggt, cgtcgaaggtacacagagat, atactgggattcggatcg, tcgctggcttagaattacat, gatcgatctgttacacga, gtagtagttagtccgat, actacacgtaggcatataga, ttcaattgtttgtttg	Stellaris smFISH probes	N/A
Pi3K21B aagcccatctgcaatatcat, tcataaagttgctgccactt, tttagcaaccagagagcttc, ctctcgtcgaatcaggaag, atggacagagcatagtgacc, agtgctgcacgatgtcttg, ggtgctcgtctcgtaaataa, gtaagggcagcaaatccaa, tctcagcgtgcatatata, gaattgttgcatagtgctc, ttctccagtcacaagacag, gatcatctgaactgacagc, tcgtactccagatccattc, catctacgacgctatgttca, agttggaggggcaaatggag, tttagcggcaattgatgtgc, gagatagatagctagcctga, gaggtagggcttagagcaa, cagccgtgtttatatctaga, ctttgacagagcctgcaaa, tactggcatatccagcttaa, gttcgtacttgcagtcattc, cgtttactagcttgatgt, atctgaatacatgttaggt, attggcagttcggacactaa, ttgtgacaaggagcctttt, ctttggctctcattactcaa, taacactaggtaacgcgtgt, ggccgaaataatagcattgc, tgctgatgtacacaatcgcc, gccatcatcacacacaaaa, aattcttgagggatagcgg, ttttctttgtttctggagc, ataccgaaaacgttttccc, agcttctagcaagctgttaa, atcacgcgaaatgcagatt, acagatagctcagcttatca, atacgggataggcggtgat, aatttctcacgatcctacc, acacgacgaaatgtgtgaa, tgctctttgttctgtttt, tcgcaaacgtttgcaagcg, cggctaggttatcaaacct, atattagagcaaggggtggg, acgtacgtagattcactta, atcaactgatcacatcagat, ttgttccgactgagtgat, tctcgtgtaaaagtctct	Stellaris smFISH probes	N/A
IRFP670-ORF cgatcacaggatgtgaggtc, tggaaactggtatgtggata, taatcgctactgcctgtgca, cctgcattttctgtgatcg, tgctcccttccaaaagaatg, cgagcaattcgccaacacgg, tccgtctcgccaaaataatc, agtgcttacggagagcgtg, cagccaaataggggcagc, aaaagtctgccagtcacat, catggcgtgcaaaactgatg, cggctcaaacctctatgatg, caatgatttgcgagtcagc, atctctcaacgacttgag, catagcctggagatagcgtg, cgaagcagatagacatcacg, ctttagcttcgcccattac, caggaacgattccaggtcac, tcaaatacagcagacggcg, tgcggaaccacacggatc, acaatgctgcaactgattcc, aactcaaatccagagctg, ccaaatgacacgggcttacc, tacgcccattttcgaaaa, tatggacagggacatgctg, cccacaaggtaccatctata, gttcgtatgatggcatatt, tacacgttgcgcatggaa, aaatccgcaaacatctctg, ggccgtgaaatgcaaggaca	Stellaris smFISH probes	N/A

(Continued on next page)

Continued

REAGENT or RESOURCE	SOURCE	IDENTIFIER
MS2 catgaggatcaccatgtct, agtattcccgggttcattag, cctaaggtacctaattgcct	Stellaris smFISH probes	N/A
EGFP tctcgccttgctcaccat, gggcaccaccccgggtaaca, cgccgtccagctcgaccagg, ctgaacttgtagccgtttac, gccctcgccctcgccggaca, tcagcttgccgttagtgggca, gtggtgcagatgaactcag, ccagggcacggcagcttg, tcagggtggtcagcagggtg, ctgaagcactgcacgcccga, cttcatgtggtcgggtagc, cggactgaagaagctgctg, tggacgtagcctcgggcat, cttgaagaagatggtgctg, gggctttagttgcccgcg, ccctgaacttcacctcggc, gatcggttcaccagggtg, ttgaagtcgatgccctcag, ccccaggatgtgcccgtcct, ttagttgtactccagctg, catgatagacgttggc, tggcgttcttctgcttgcg, cggatctgaagttcacct, gctgccgtcctgatgtgt, tggtagtggcggcagctg, gtcgccgatgggggtgtct, ttgctggcagcagcacggg, ggactgggtgctcaggtag, cgtggggtcttggctcagg, aggaccatgtgatcgcgctt, ggcggcggtcacgaactcca, tgcctcatgccgagagtgat	Stellaris smFISH probes	N/A
<i>osk</i> , <i>nos</i> , <i>CycB</i> , <i>gcl</i> and <i>GFP</i> probes were described previously	(Trcek et al., 2015)	
STORM smFISH Probes (5' to 3')		
<i>nos</i> dSTORM3: ggtaaagctacgcgccaact (Alexa647; 5'UTR)	IDT Technologies	N/A
<i>nos</i> dSTORM4: aagcacagttattcaactg (Alexa647; 5'UTR)	IDT Technologies	N/A
<i>nos</i> dSTORM5,7: ccaggcgctatttaaactgt (Alexa 647; 3'UTR)	IDT Technologies	N/A
<i>nos</i> dSTORM6, 8: ttttcagaatagtgtacac (Alexa647; 3'UTR)	IDT Technologies	N/A
<i>nos</i> dSTORM9, 10: cgagattggtggacacagtg (Alexa568; middle ORF)	IDT Technologies	N/A
<i>nos</i> dSTORM11: gtttcccttcacagaaaca (Alexa647; 3'UTR)	IDT Technologies	N/A
<i>nos</i> dSTORM12: tgatagattgacagttcga (Alexa647; 3'UTR)	IDT Technologies	N/A
<i>gcl</i> dSTORM1: gggacagtaattacatgcgt (Alexa568; 5'UTR) (cross-correlation)	IDT Technologies	N/A
<i>gcl</i> dSTORM4: acttgtaaaactgcagttac (Alexa647; 5'UTR)	IDT Technologies	N/A
<i>gcl</i> dSTORM6: gcggatagcttatactcga (Alexa647; 3'UTR)	IDT Technologies	N/A
<i>gcl</i> dSTORM7: cgaactgctcgggtaaatg (Alexa647; 3'UTR)	IDT Technologies	N/A
<i>gcl</i> dSTORM8: ccgacgaatggtcagctac (Alexa647; middle ORF)	IDT Technologies	N/A
<i>gcl</i> dSTORM9: tggaaaccaagacagcatcc (Alexa647; beginning ORF)	IDT Technologies	N/A
<i>osk</i> dSTORM1: aatcgcgcaaatgcttact (Alexa647; 3'UTR, next to the stem loop)	IDT Technologies	N/A
<i>osk</i> dSTORM2: caataactgcagtagcgc (Alexa647; end of ORF)	IDT Technologies	N/A
<i>osk</i> dSTORM3: gatctgaaccaaaagccttg (Alexa568; middle ORF)	IDT Technologies	N/A
<i>osk</i> dSTORM4: ggaattcactgtgactgctg (Alexa568; 5'UTR)	IDT Technologies	N/A
<i>osk</i> dSTORM5: caggaaatccgtcagttgt (Alexa647; beginning ORF)	IDT Technologies	N/A
<i>osk</i> dSTORM6: attacggccaaaatgcagca (Alexa647; 3'UTR next to the stem loop)	IDT Technologies	N/A
<i>Osk</i> dSTORM7: tacacagctttgggatagc (Alexa647; 3'UTR)	IDT Technologies	N/A
<i>CycB</i> dSTORM3: gttttgtatgaatgctcga (Alexa647; 3'UTR) (cross-correlation)	IDT Technologies	N/A
Oligonucleotides		
<i>nos</i> Fw: acctacgtggtccccatctg	IDT Technologies	N/A
<i>nos</i> Rv: ttccgccttgatcgcacatct	IDT Technologies	N/A
<i>gcl</i> Fw: tgactctgagccttcgacgc	IDT Technologies	N/A
<i>gcl</i> Rv: cgccagttgtccgcagattg	IDT Technologies	N/A
<i>CycB</i> Fw: cgcccactctgacctctac	IDT Technologies	N/A
<i>CycB</i> Rv: ttgaccgcactatttctc	IDT Technologies	N/A
<i>DMN</i> Fw: agacgcctggaagtaagcag	IDT Technologies	N/A
<i>DMN</i> Rv: gtaaggcggtcaactgtc	IDT Technologies	N/A

(Continued on next page)

Continued

REAGENT or RESOURCE	SOURCE	IDENTIFIER
Recombinant DNA		
IRF670	Addgene	45457
Gal4-responsive UASp promoter plasmid	(Rørth, 1998)	N/A
Software and Algorithms		
https://www.biosearchtech.com/Account/Login?return=/stellaris-designer	LGC Biosearch technologies	N/A
Airlocalize spot detection algorithm	(Trcek et al., 2017; Lionnet et al., 2011)	
PCC(Costes) co-localization ImageJ plugin	(Bolte and Cordelières, 2006)	JACoP ImageJ
Sigmaplot	https://systatsoftware.com/	N/A
Script for pair-correlation analysis	(Veatch et al., 2012)	MATLAB
Script for auto-correlation analysis	(Sengupta et al., 2011)	MATLAB

RESOURCE AVAILABILITY**Lead Contact**

Further information about this work should be directed to the lead contact, Ruth Lehmann (ruth.lehmann@med.nyu.edu) and co-corresponding author Tatjana Trcek (ttrcekp1@jhu.edu).

Materials Availability

Requests for resources and reagents should be directed and will be fulfilled by the lead contact, Ruth Lehmann (ruth.lehmann@med.nyu.edu) and co-corresponding author Tatjana Trcek (ttrcekp1@jhu.edu). All unique reagents generated in this study are available from the Lead Contact and co-corresponding author without restriction.

Data and Code Availability

Requests for data and codes generated in this study should be directed and will be fulfilled by the lead contact, Ruth Lehmann (ruth.lehmann@med.nyu.edu) and co-corresponding author Tatjana Trcek (ttrcekp1@jhu.edu). Original data have been deposited to Mendele Data: <https://doi.org/10.17632/h4wfnfsgw8.1>.

EXPERIMENTAL MODEL AND SUBJECT DETAILS**Fly lines**

Flies were maintained on cornmeal molasses/yeast medium at RT or 25°C using standard procedures. To create the *nos* chimeras described in this study, the 5'UTR of *nos* was fused with the *Drosophila* codon optimized ORF sequence of the near-infrared fluorescent protein IRF670 (Addgene, #45457) and *nos* 3'UTR. The expression of this chimera was driven by the *nos* promoter (Rangan et al., 2009). Alternatively, the IRF670 ORF and *nos* 3'UTR were fused with the 5'UTR of P element transposase gene and driven by the Gal4-responsive UASp promoter (Rørth, 1998). These two constructs were inserted into the attP40 site (2nd chromosome) via the PhiC31 integrase-mediated site-specific integration by Best Gene.

METHOD DETAILS**Microscopes**

Unless otherwise specified, images were acquired with an instant Structural Illumination Microscope (iSIM) (Curd et al., 2015; York et al., 2013) in 3D with a 150nm Z step as previously described (Trcek et al., 2017). Using Huygens (Scientific Volume Imaging), images were deconvolved and corrected in 3D for chromatic aberrations using multicolored beads (ThermoFisher Scientific; T7279) (Trcek et al., 2015, 2017).

To image co-localization of *nosp-5'gcl-EGFP-3'gcl* and *nosp-5'pgc-EGFP-3'pgc* chimeras with endogenous *gcl* or *pgc* a Nikon Structured Illumination Microscope using a 100x 1.5 NA oil immersion objective, with pixels of 33 × 33 nm was used (Eagle et al., 2018). For each embryo, a z series of 21 slices was taken, with a step size of 150 nm. To minimize fluorescent signal distortion, all images were taken within 5 μm of the embryo cortex.

For FRAP assays, a Zeiss LSM780, AxioObserver inverted, laser scanning confocal microscope, equipped with an argon, an HeNe 633 laser and a DPSS 561-10 laser, a Plan-Apo40X/1.4 Oil DIC and EC Plan-Neofluar 10X/0.30 objectives was used.

To quantify *nos* and *pgc* mRNA levels in the soma and in the germ plasm through early embryogenesis (Figures S3F and S3G), an API DeltaVision personal DV widefield epifluorescence microscope equipped with the Photometrics CoolSNAP HQ2 CCD camera and Olympus PlanApo N 60X/1.42 oil and UPlanSApo 20X/0.75 objectives was used (Trcek et al., 2015).

For auto-correlation experiments, a custom Stochastic Optical Reconstruction Microscope (STORM) was used. The system was built on an optical imaging platform equipped with the Leica DMI 3000 inverted microscope, 488-nm (OBIS, Coherent) and 639-nm (MRL-FN-639-800, CNI) laser lines, as previously described (Nemoz et al., 2018). Laser lines were reflected into an HCX PL APO 63X NA = 1.47 OIL CORR TIRF Objective (Zeiss) by a penta-edged dichroic beam splitter (FF408/504/581/667/762-Di01-22x29). Afterward, the emitted fluorescence was extended by a 2X lens tube (Diagnostic Instruments), filtered by single-band filters (Semrock FF01-531/40, FF01-607/36, and FF01-676/37 for GFP, Alexa Fluor 568, and Alexa Fluor 647, respectively), and collected onto a scientific (sCMOS) camera (Prime95B, Photometrics). To reactivate Alexa Fluor647 fluorophores, the microscope was also equipped with a 405-nm laser line (MDL-III-405-150, CNI). To achieve super-resolution imaging, the 561 and 639 laser lines were adjusted to ~1.0 and 1.5 kW cm⁻², and a highly inclined and laminated optical sheet illumination mode was used for sample excitation. Alexa568 and Alexa647 dyes were sequentially excited and their emitted fluorescence sequentially collected by switching the single-band filters in a filter wheel. A minimum of 2,000 frames at 33 Hz were recorded for each image stack (Nemoz et al., 2018).

For cross-correlation experiments a second Stochastic Optical Reconstruction Microscope (STORM) was used. This system was built on a Leica DMI 3000 inverted microscope base (Whelan et al., 2018). In brief, the 473 nm (Opto Engine LLC, MBL-473-300 mW), 532 nm (OEM Laser Systems, MLL-III 200 mW), and 640 nm (OEM Laser Systems, MLL-III 150 mW) laser beams were collimated and reflected into an HCX PL APO 100x NA = 1.47 TIRF objective (Leica) via a multi-band dichroic (Chroma, zt405/488/532/640/730rpc, UF1C165837). The illumination was adjusted into a Highly Inclined and Laminated Optical (HILO) illumination mode to achieve an image depth of ~400 – 600 nm. Multi-color imaging was achieved by sequentially imaging different fluorophores. Emitted fluorescence was collected with the same objective and further filtered by single-band filters (Semrock FF01-531/40, FF01-607/36, and FF01-676/37 for GFP, Alexa Fluor 568, and Alexa Fluor 647, respectively) switched in a filter wheel (Thorlabs, FW102C) accordingly. The photons from each color were then recorded on an EMCCD (Andor iXon +897) at 33Hz for 2000 frames with an EM gain of 300. Note that the microscope was also equipped with a 405 nm laser line (MDL-III-405-150, CNI) to reactivate Alexa Fluor 647. A minimum of 2,000 frames at 33 Hz were recorded for each image stack.

Embryo collection

Unless otherwise noted, caged flies were allowed to lay eggs at room temperature (RT) on a fresh apple juice plate containing a dollop of fresh yeast paste for 1.5 hours, after which the embryos were dechorionated and the vitelline membrane removed by methanol cracking. Embryos were then stored in 100% methanol at 4°C until further use (Trcek et al., 2015, 2017).

Single-molecule fluorescent *in situ* hybridization (smFISH)

A mix of commercially-available Stellaris smFISH probes was used to label individual mRNAs (Key Resources Table) (Trcek et al., 2015, 2017). The probes were designed as 20 nucleotides long DNA primers and covalently coupled to a CAL Fluor 590 dye (<https://www.biosearchtech.com/Account/Login?return=/stellaris-designer>). To prepare Alexa488-labeled smFISH probes, the probes were AmMC12 modified at the 5' end (IDT Technologies), labeled using the AlexaFluor 488 oligonucleotide Amine labeling kit and purified using the MicroSpin G-25 Columns (Trcek et al., 2015, 2017). Hybridization of mRNAs with smFISH probes was carried out as described before (Trcek et al., 2015, 2017).

mRNA concentration and cluster abundance measurements using smFISH

Somatic mRNA concentrations were quantified as described previously (Trcek et al., 2015). In short, using iSIM, the images of smFISH-labeled embryos were acquired in 3D with a 150 nm Z step. A 3D ROI with known spatial dimensions was then chosen outside of the *Vasa*:GFP stain (Figures S1A and S1B, yellow square labeled “Soma”), which demarcated the germ plasm boundaries. The absolute number of smFISH-labeled mRNAs within the 3D ROI was determined and finally, the nM concentration of mRNAs in the 3D ROI and hence in the embryo calculated (Trcek et al., 2015, 2017). We observed a high correlation between the relative expression levels determined by RNA-sequencing (Roy et al., 2010) and the somatic concentration determined by smFISH for the mRNAs tested ($R^2 = 0.85$; Figures S1E and S1F), indicating that smFISH quantified mRNA concentrations over a wide gene expression range, as demonstrated previously (Trcek et al., 2015, 2017).

Because of the high somatic *CycB* expression, smFISH could not be used to quantify somatic concentration of this mRNA reliably and we instead estimated it. As noted above, we observed a linear relationship between the mRNA concentration determined by smFISH and the mRNA levels determined by RNA-seq (Figure S1E, formula). Using this linear relationship and *CycB* mRNA levels determined by RNA-seq (Flybase (Roy et al., 2010)), we extrapolated the somatic concentration of *CycB* mRNA to be 12.46 nM (Table S1, marked as *).

To determine the mRNA concentration in the germ plasm (GP), we analyzed a 3D ROI with known spatial dimensions demarcated by the *Vasa*:GFP stain, which identified the germ granule-bound mRNAs (Figures S1A and S1B, yellow square labeled “GP” (germ plasm)). The number of smFISH-labeled spots per 3D GP ROI was then determined and their intensity normalized by the intensity of a single smFISH-labeled mRNA located in the soma to determine the absolute number of transcripts per 3D ROI (Trcek et al., 2015, 2017). The spatial dimensions of the 3D ROI were then used to calculate the nM mRNA concentration in GP (Table S1).

To determine the abundance of mRNA clusters (average number of mRNAs per homotypic cluster) in germ granules, we analyzed a 3D ROI as described above. For each embryo, we measured the number of smFISH-labeled mRNA clusters within the 3D GP ROI and afterward determined the number of mRNAs in each cluster by normalizing its fluorescent intensity to the intensity of a single smFISH-labeled mRNA located in the somatic regions of the embryo (Figures S1A and S1B, yellow square labeled “Soma”) (Trcek et al., 2015, 2017). At least three embryos per mRNA were analyzed this way, and the average mRNA cluster abundance among all analyzed clusters determined.

Importantly, we found that up to the periphery of the germ plasm, where germ granules meet the somatic regions of the embryo, the number of Vasa:GFP granules increased linearly with the size of 3D ROIs (Figures S1C and S1D, magenta dotted line in Figure S1D) indicating that germ granules are homogeneously distributed within the germ plasm. Therefore, the mRNA concentration in germ plasm and the average abundance of mRNA clusters were invariant of the size of the 3D ROIs.

To determine the abundance of *CycB* clusters in GP, we first estimated the total fluorescence intensity of a single somatic *CycB* mRNA. We calculated the somatic concentration of *CycB* as described above and afterward estimated the number of *CycB* molecules per 3D ROI of known spatial dimensions in the soma. We then quantified the total fluorescence intensity of somatic *CycB* within a 3D ROI and divided this number by the number of *CycB* within this ROI to obtain an estimate for the fluorescence intensity of a single somatic *CycB*. This value was then used to normalize the fluorescence intensity of *CycB* smFISH labeled mRNA spots in the GP to determine the concentration of *CycB* and *CycB* cluster abundance in the germ plasm.

Correlating mRNA properties with the position of mRNA clusters in germ granules

To determine which mRNA property best predicted the position of clusters within granules, we correlated several mRNA parameters with the spatial position of homotypic clusters within Vasa:GFP-labeled granules, we used the PCC(Costes) approach (Trcek et al., 2015). We found that timing of translational onset in germ granules (Rangan et al., 2009), susceptibility to mRNA decay in the somatic regions of the embryo (Thomsen et al., 2010), and length of their 3'UTR (Roy et al., 2010) had little effect on cluster positioning. For example, mRNAs that were translationally repressed in granules were as likely positioned at the edge of the granule (*gcl*) as in the center of the granules (*CycB*) (Trcek et al., 2015). To directly address whether the translational status of a localized mRNA alters its position in the granule, we made use of the known function of Nanos protein as a translational repressor of *CycB* mRNA translation. In the absence of Nos, localized *CycB* becomes precociously translated (Kadyrova et al., 2007; Sonoda and Wharton, 2001), however, the position of *CycB* clusters in Vasa:GFP-labeled granules did not change (Figures S2C and S2D). This supports the conclusion that the translational status of mRNAs within granules does not inform cluster position. This result also indicates that the removal of even abundant RNA clusters such as *nos* did not affect the spatial position of other mRNAs clusters.

Next we found that an mRNA's translational efficiency in the cytoplasm of oocytes, during the period when mRNAs enrich into granules, and at the end of oogenesis, when mRNA enrichment to granules is complete, is correlated negatively with the positioning of mRNA clusters (Kronja et al., 2014; Little et al., 2015). These measurements of mRNAs in heavy polysomal fractions largely account for the RNA pool that will end up in the somatic region of the embryo as germ granule mRNAs only account for approximately 3% of total mRNA (Trcek et al., 2015; Bergsten and Gavis, 1999) and suggested that mRNAs that translated less efficiently in the oocyte cytoplasm tend to position more centrally within granules, while those that translated more efficiently positioned toward the granule periphery (Figure S2A). Similarly, mRNA length had a moderately negative effect on position, with longer mRNAs showing a preference to be positioned at the edge of the granule (Figure S2A). Finally, we found that the best predictor of mRNA cluster position in *Drosophila* germ granules were the somatic concentration of a transcript in the embryo, its germ plasm (GP) concentration in the embryo, fold enrichment (the ratio between the GP and the somatic mRNA concentration in the embryo), and mRNA cluster abundance (see main text and Figures 1G, S2A, and S2B).

Correlating mRNA cluster abundance with the abundance of granule proteins

To generate correlations between smFISH-labeled mRNAs and fluorescently-tagged proteins, two-dimensional ROIs within germ plasm from each fluorescent channel were analyzed using Airlocalize, which generated an array of XY coordinates and the fluorescent intensity occurring at each coordinate for both channels (two arrays total, one per channel) (Trcek et al., 2017). The distances between all coordinates across these two arrays were calculated, and coordinates that occurred within 400nm of each other were identified as occurring within the same granule. The intensities of any two coordinates co-localizing to the same granule were paired together. Coordinates that did not co-localize to the same granule with any spot from the alternative channel were paired with a zero intensity value for the other channel. Finally, a Pearson's correlation was calculated between all paired intensity values between the two channels, producing a measure of how granule components correlated with each other per granule across all granules within a germ plasm ROI. Our analysis revealed that only 44.2% of the variability in the abundance of *nos* clusters could be explained by the variability in Osk protein abundance (Figures 1E and S1G), an RBP previously implicated in recruitment of *nos* to germ granules (Yang et al., 2015; Jeske et al., 2015). This correlation was even smaller when the *nos* cluster abundance was correlated with the abundance of Vasa and Tud and negative when correlated with the abundance of Aub (Figures 1F and S1G). Notably, the correlation between *nos* and Vasa was nearly equivalent to the correlation between *pgc* and *gcl* mRNA clusters, two mRNAs that enrich in granules independently of one another (Figure S1G).

Quantifying co-localization using PCC(Costes)

Co-localization between overlapping mRNA clusters and Vasa:GFP granules and mRNA clusters labeled with spectrally-distinct fluorophores was quantified in 3D ROIs using the Pearson Correlation Coefficient-Costes approach (here termed PCC(Costes)), as previously described (Trcek et al., 2015). PCC(Costes) measures co-localization by determining how fluorescence intensities of labeled objects spatially correlate with each other within the overlap and afterward statistically evaluates the significance of this co-localization (Costes et al., 2004; Bolte and Cordelières, 2006). PCC(Costes) of 1.0 indicates perfect, non-random co-localization while PCC(Costes) of ~0.0 indicates that two objects labeled with spectrally-distinct dyes co-localize with each other by chance (Costes et al., 2004; Bolte and Cordelières, 2006). PCC(Costes) is insensitive to the frequency and the duration of overlap between objects and therefore measures co-localization even in crowded cellular environments such as germ plasm (Trcek et al., 2015; Costes et al., 2004; Bolte and Cordelières, 2006). To establish PCC(Costes) as a method to analyze co-localization further, we have previously employed a spot detection algorithm to quantify nm distance between the centers of mass of overlapping objects labeled with spectrally distinct fluorophores (Trcek et al., 2015). We demonstrated that as the PCC(Costes) coefficient decreases, the distance between overlapping objects labeled with spectrally distinct colors increases indicating that the two objects co-localize at a greater yet fixed spatial distance relative to each other (Trcek et al., 2015; Bolte and Cordelières, 2006; Costes et al., 2004). Additionally, we have previously determined the upper limit of co-localization detection using the double-labeled *pgc* mRNA and measured a high PCC(Costes) of 0.90 ± 0.004 and a distance of 33.1 ± 5.1 nm (Trcek et al., 2015). We detected a similar co-localization for Osk:GFP and Vasa:KuOr proteins (PCC(Costes) of 0.93 ± 0.01 ; distance of 30.6 ± 4.3 nm (Trcek et al., 2015)) and therefore concluded that Oskar and Vasa were homogeneously mixed within granules. In contrast, a non-granule-enriched *ccr4* mRNA randomly co-localized with Vasa:GFP-labeled germ granules with a PCC(Costes) of 0.04 ± 0.02 and at a spatial distance of 408.5 ± 31.4 nm (Table S1) (Trcek et al., 2015), indicating that *ccr4* randomly co-localizes with germ granules and was not a granule component (Trcek et al., 2015).

To determine how endogenous *nos* co-localizes with itself and determine the upper limit of co-localization detection using PCC(Costes) in Figure 3A, we prepared two sets of *nos* probes that had the same sequences but were labeled with either green or red probes. We mixed them together and labeled the *nos* mRNA clusters concurrently and therefore variably. This approach best simulated the variability that can arise due to different mRNA composition of different chimeras *in vivo*. Nevertheless, in this control, we achieved high PCC(Costes) of 0.84 ± 0.01 indicating that the variability in probe hybridization or probe on and off rates add minimally to the noise of the measurements and do not obscure the underlying spatial organization of the molecules within clusters.

Quantifying total embryonic mRNA levels using qRT-PCR

To determine total embryonic mRNA levels using qRT-PCR, caged flies were provided with a fresh apple juice plate containing a dollop of fresh yeast paste and allowed to lay eggs for 1.5h hours. After dechoriation, the embryos were resuspended in 100 μ l of 1XPBS and 800 μ l TRIzol reagent (Invitrogen; 15596018) and broken up using a pellet pestle motor (Kimble Kontes). The RNA was then extracted with the acid-phenol:chloroform (Invitrogen; AM9720), followed by one extraction with chloroform (Fisher; AC40463-5000) and one extraction with isopropanol (Fisher Scientific; A416-500) (Köhler and Domdey, 1991). The RNA was precipitated to the bottom of the tube during a 15 min spin at maximal speed at 4°C. Isopropanol was then removed, the RNA was washed once with 70% ethanol, air-dried and resuspended in nuclease free water. DNA contaminations were removed with RQ1 RNase-Free DNase (Promega; M6101). Afterward, the RNA was re-purified using the acid-phenol:chloroform extraction, as described above. 5 μ g of total RNA was transcribed into cDNA in the reverse transcriptase reaction using Oligo dT(20) primer (Thermo Fisher Scientific; 18418020) and the SuperScript® III Reverse Transcriptase (Life Technologies; 18080-044). Relative differences in mRNA concentrations we determined using a comparative C_T method for relative quantification by RT-PCR (Livak and Schmittgen, 2001). SYBR Green was used as a reporter dye (Roche; 04707516001). The reactions were set up in 384-well qRT-PCR plates (Roche; 04729749001) in three biological and four technical replicates for each RNAi condition and for each gene. qRT-PCR was performed using the Roche LightCycler® 480 II system and a standard qRT-PCR program. The reaction was carried out using 1 μ l of cDNA (1:3 dilution), and 300 nM of Fw and Rv and 5 μ l SYBR Green PCR mix. Dissociation curves generated through a thermal denaturation step were used to verify amplification specificity. A sample with no reverse transcriptase was used as a negative control. DMN gene was used to normalize RNA levels. The gene specific primers used in the qRT-PCR reaction are provided in the Key Resources Table. Transcription of the GAL4 inducer, which triggered expression of the RNAi against *CycB*, *nos* or *mCherry*, was achieved by the maternal *alpha tubulin* promoter (*mat-alpha*) (Staller et al., 2013).

Fluorescence recovery after photobleaching (FRAP)

FRAP was used to evaluate the kinetics of exchange of fluorescently-tagged granule components Osk, Vasa, Aub and Tud and *nos* mRNA with the intergranular space. To detect *nos* mRNA in FRAP experiments, we used a *nos* transgene that was genetically engineered with 18 tandemly-repeated RNA loops derived from the MS2 bacteriophage (Brechtel and Gavis, 2008). These repeats accommodate co-transcriptional labeling of the RNA with the GFP-tagged MS2 coat protein (MCP-GFP) (Bertrand et al., 1998; Tuccini et al., 2018), allowing *nos* detection in live embryos (Figures 2B and 2C) (Sinsimer et al., 2013). *nos*-MS2-MCP-GFP mRNA forms clusters of similar abundance as WT *nos* (Figure S3A) and rescues the *nos* null phenotype (see below) (Forrest et al., 2004) indicating that the essential features of *nos* regulation are recapitulated on this chimeric mRNA. Live embryos were prepared and mounted onto an imaging chamber as described before (Kistler et al., 2018). Per embryo, a 3 μ m X 3 μ m 2D ROI was photo-bleached in the middle of

the germ plasm, where germ granules were homogeneously distributed within the germ plasm (Figures S1C and S1D). Since germ granules are too small to allow photo-bleaching of individual granules, we instead photo-bleached a larger ROI in the middle of the germ plasm, where germ granules are homogeneously distributed within the germ plasm (Figures S1C and S1D). We have previously shown that up to 7% of Osk and Vasa resides in the intergranular space, that approximately 40% of Osk and Vasa found in granules exchange with the intergranular space and that the rest does not exchange and remains associated within granules (Kistler et al., 2018). Thus, we anticipated capturing the behavior of at least three populations of fluorescently-tagged molecules with distinct kinetics of fluorescence recovery (Figure S3B); population P1 located in the intergranular space with fast mobility (M1), population P2 located within granules that is exchanging with the intergranular space with a slow mobility (M2) and population P3 found within granules that does not exchange with the intergranular space (immobile fraction). To capture the kinetic of exchange of three populations of fluorescently-tagged molecules with distinct kinetics of fluorescence recovery (Figure 3B), the FRAP recovery curves were first normalized as described before (Kistler et al., 2018; Brangwynne et al., 2009; Rapsomaniki et al., 2012). Afterward, the recovery curves were fit to a two-term exponential equation ($f(t) = a*(1-\exp(-b*t)) + c*(1-\exp(-d*t))$) using Sigmaplot (<https://systatsoftware.com/>), where a and c represented the percent mobile fractions (Figure S3B; Table S2; population P1 and P2), and b and d represented the rate constants of fluorescence recovery. b and d were then used to calculate the half time to full fluorescence recovery $t_{1/2}$ (s) using the equation $b = \ln(2)/t_{1/2}$ (Figure S3B; Table S2; mobility M1 and M2) (Rapsomaniki et al., 2012; Brangwynne et al., 2009; Kistler et al., 2018). To statistically evaluate, whether a two-term exponential equation was more appropriate to describe our FRAP data than a single-term exponential equation ($f(t) = a*(1-\exp(-b*t))$) (Kistler et al., 2018), we used both the F-test and the Normality Test (Shapiro-Wilk). By doing so, we determined that the FRAP recoveries of Osk:GFP, Vasa:GFP, Aub:GFP, Tud:GFP and nos-MS2-MCP-GFP were best described using a two-term exponential equation while the FRAP recoveries of a GFP and MCP-GFP expressed in the absence of the MS2-tagged nos, were best described using a single-term exponential equation (Table S2).

Hybridizing cut embryos with smFISH probes for imaging with STORM

Vasa:GFP-expressing embryos were fixed, devitellinized and stored in 100% methanol at 4°C until needed, as described previously (Trcek et al., 2017). Afterward, embryos were rehydrated as described before (Trcek et al., 2017). Afterward they were resuspended in 1X phosphate-buffered saline (PBS) and laid into plastic disposable molds (Fisherbrand; 22-363-552) to achieve a single and uniform layer of embryos at the bottom of the mold. The buffer was then removed and the molds with the embryos filled with the tissue freezing medium (General Data; TFM-C). Embryos were frozen immediately on dry ice. Frozen and embedded embryos were then cut with a 10 μm Z step using a cryostat (Leica; CM 3050 S) at -19°C using pre-chilled low profile blades (Accu-Edge; 4689). Each cut slice was affixed onto microscope coverslips coated with the Poly-L-lysine solution (Sigma; P4707-50ml) and steeped in 1XPBS for 5 min. Afterward, the cut embryos were post-fixed with 4% paraformaldehyde (Trcek et al., 2017) for 5 minutes, washed once with 1XPBS (5 min) and hybridized with smFISH probes or stored O/N at 4°C and used the next day. Freezing and cutting of the embryos did not alter how *CycB* and *gcl* mRNA clusters co-localized with Vasa:GFP granules (Figure S4F), indicating that the spatial dimensions of germ granules were preserved during sample preparation. Cut embryo slices attached onto the coverslips were steeped into a pre-hybridization solution containing 10% deionized formamide and 1X saline-sodium citrate (SSC) buffer (Trcek et al., 2017) for 15 min. Afterward, coverslips were placed face-down onto 30 μl of hybridization solution containing smFISH probes (see below) within the hybridization chamber. This chamber comprised of a 10 cm Petri dish, a parafilm strip placed into the Petri dish and a falcon tube cap filled with the pre-hybridization solution to humidify the chamber (Trcek et al., 2012). The chamber was sealed with parafilm, and into a 37°C incubator for 3h shielded from light. Afterward, the coverslips were washed twice with pre-hybridization solution pre-warmed to 37°C for 15 min, followed by two 5 min washes with 1XPBS at RT.

To prepare the smFISH-containing hybridization solution for STORM imaging, the same protocol was used as described previously (Trcek et al., 2017), but instead of a mix of probes designed to hybridize along the entire length of the mRNA target, a single smFISH probe covalently modified at its 5' end with Alexa 568 or Alexa647 photoswitchable dye was used per mRNA. These probes were custom design using the Stellaris designer (Biosearch Technologies) and then fluorescently-modified and purchased from Integrated DNA Technologies (Key Resources Table).

Imaging of smFISH-labeled samples using STORM

Hybridized samples were mounted onto a perforated microscope slide and sealed with Epoxy (Devcon; 00470740). Samples were then perfused with 100 μl of 1XPBS containing 10% glucose and 1 μl of Gloxy anti-bleach solution (100 μl of Gloxy contains 80 μl 1XPBS, 20 μl Catalase (Sigma-Aldrich; C3115-50MG) and 10 mg Glucose Oxidase (Sigma-Aldrich; G2133-10KU)). Per embryo, 2000 images were acquired in 2D at the rate of 30 Hz.

We individually hybridized mRNAs with smFISH probes coupled with photoswitchable Alexa568 or Alexa647 dyes (Key Resources Table), while Vasa:GFP continued to demarcate the position of germ granule-bound mRNA clusters (Figures S4A–S4D, magenta ROI). After image acquisition (Video S1), particles were detected and images reconstructed (Figure S4E). Our imaging approach revealed bright, distinct and frequent photoswitchable events of fluorescently-labeled probes (Video S1) indicating that after the initial inactivation of fluorophores, a sparse subset of dyes was activated into a fluorescent state thereby markedly increasing our ability to determine precise positions of smFISH-hybridized mRNAs with low localization uncertainty. An ROI coinciding with the Vasa:GFP label was cropped from reconstructed images (Figure S4E, magenta ROI) and analyzed to plot the distances among all detected fluorescently-labeled mRNAs (Figures S4D and S4E, black dots). Since clusters do not form outside of germ granules and the

vast majority of clusters contained more than one mRNA (Tables S1 and S6), the plot of distances represented the spatial dimensions of homotypic mRNA clusters. By fitting this data to an auto-correlation function (Sengupta et al., 2011) (Figure S4E, violet line), we extracted the radii (in nm) of mRNA clusters reported by a particular smFISH probe. Notably, the radii represented the physical size of an mRNA cluster rather than the physical dimension of a *trans* RNA:RNA interaction. Finally, we further validate STORM as a method to detect the spatial organization of clustered mRNAs by investigated the co-localization of *CycB* clusters with *gcl* clusters (Figures S4J–S4L). Using cross-correlation analysis (Veatch et al., 2012) we determined that the mean distance between *CycB* and *gcl* clusters in germ granules to be 134.9 ± 90.3 nm (Figure S4L), a distance similar to our previous measurement of 78.9 ± 8.1 obtained with smFISH and iSIM approach (Trcek et al., 2015), confirming that *CycB* and *gcl* mRNAs organized homotypic clusters within the same germ granule.

Importantly, this distance was shorter than the 250 nm radius of the granule observed by EM (Arkov et al., 2006; Mahowald, 2001), yet longer than the average radius of 62.8 ± 2.3 nm and 35.4 ± 2.3 nm for *CycB* and *gcl* mRNA clusters, respectively (Figure S4L). This result indicated that *CycB* and *gcl* mRNAs do not mix with each other within the same granule, but instead occupy distinct positions, confirming our previous measurements (Figure 1G) (Trcek et al., 2015). Finally, we observed a flat cross-correlation curve for *CycB* and *gcl* mRNAs in the somatic regions of the embryo indicating that in the soma, all detected distances among these two mRNAs were equally likely (Figure S4K). Therefore, outside of germ granules, *CycB* and *gcl* randomly co-localized with each other, consistent with previous observations (Trcek et al., 2015).

Single-Molecule Localization

For STORM taken via the sCMOS camera, the single-molecule localization procedure was carried out as previously described (Yin et al., 2019). Briefly, raw STORM images were box-filtered with a box size of 4x FWHM of a 2D PSF, and with each pixel within the box weighted by the inverse of its variance (Huang et al., 2013). A 9x9 pixel regions around each local maximum of the filtered images were then submitted for single-molecule localization. The single-molecule localization was achieved by fitting each single PSF into a 2D Gaussian profile via Maximum Likelihood Estimation (MLE), and the fitting accuracy was determined by the Cramér-Rao Lower Bound (CRLB) when the fitting reached the termination criteria ($p = 0.05$). Note that the readout noise of each pixel was considered as a normal distribution with its offset, variance, and gain pre-calibrated (Huang et al., 2013). The centers of the single-molecule localizations that appeared in consecutive frames within 2.5x localization precisions were considered as one blinking event. The resulting coordinates of the single-molecule centers were then submitted for Auto-Pair-Correlation analyses.

Pair-Correlation Analysis

Binary images $I_{CHx}(r)$ were submitted to a custom-written MATLAB script for pair-correlation analysis. The pair-correlation function was computed as (Veatch et al., 2012):

$$g(\mathbf{r}) = \frac{1}{N\rho_{CH1}\rho_{CH2}} \mathcal{F}^{-1}[\mathcal{F}(I_{CH1}(\mathbf{r}))\mathcal{F}^*(I_{CH2}(\mathbf{r}))]$$

where \mathcal{F} and \mathcal{F}^{-1} denotes Fourier and inverse Fourier transform, respectively. * denotes complex conjugation; ρ_{CHx} denotes the average density (number of localizations / image size) from channel x; and N is the normalization factor (Veatch et al., 2012). Note that the auto-correlation was computed by taking CH1 and CH2 as the same channel.

The auto-correlation was fitted as (Sengupta et al., 2011)

$$g(r) = \frac{1}{4\pi\sigma^2\rho} \exp\left(-\frac{r^2}{4\sigma^2}\right) + A \exp\left[-\frac{r^2}{4(\sigma^2 + r_{app}^2)}\right] + 1$$

where σ denotes the localization accuracy; $\langle\rho\rangle$ denotes the average density of molecules after over-counting correction; r_{app} denotes the apparent average radius of the clusters; and A denotes the compaction factor. The average molecular content of each cluster N was calculated as

$$N = \int_{-\infty}^{+\infty} \int_{-\infty}^{+\infty} \rho A \exp\left(-\frac{x^2 + y^2}{2r_{app}^2}\right) dx dy = 2\pi\rho A r_{app}^2$$

The cross-correlation was fitted as

$$c(r) = A \exp\left(-\frac{r^2}{2d_{app}^2}\right) + 1$$

where d_{app} denotes the apparent average distance between correlation pairs.

QUANTIFICATION AND STATISTICAL ANALYSIS

Representative images are shown for all experiments. All experiments were repeated at least three independent times unless indicated otherwise. Statistical analysis was performed using Sigmaplot. Two-tailed Student t test was used to determine significance.